An Hα search for overdense regions at $z = 2.23$[⋆]

Y. Matsuda,[1]† Ian Smail,[2] J. E. Geach,[3] P. N. Best,[4] D. Sobral,[4] I. Tanaka,[5] F. Nakata,[5]
K. Ohta,[6] J. Kurk,[7] I. Iwata,[5] Rich Bielby,[1] J. L. Wardlow,[8] R. G. Bower,[2]
R. J. Ivison,[4,9] T. Kodama,[5] T. Yamada,[10] K. Mawatari[10] and M. Casali[11]

[1]*Department of Physics, Durham University, South Road, Durham DH1 3LE*
[2]*Institute for Computational Cosmology, Durham University, South Road, Durham DH1 3LE*
[3]*Department of Physics, McGill University, 3600 Rue University, Montreal, QC H3A 2T8, Canada*
[4]*SUPA, Institute for Astronomy, Royal Observatory of Edinburgh, Blackford Hill, Edinburgh EH9 3HJ*
[5]*Subaru Telescope, National Astronomical Observatory of Japan, 650 North A'ohoku Place Hilo, HI 96720, USA*
[6]*Department of Astronomy, Kyoto University, Kyoto 606-8502, Japan*
[7]*Max-Planck-Institut für Extraterrestrische Physik, Postfach 1312, 85741 Garching, Germany*
[8]*Department of Physics and Astronomy, University of California, Irvine, CA 92697, USA*
[9]*UK Astronomy Technology Centre, Royal Observatory, Blackford Hill, Edinburgh EH9 3HJ*
[10]*Astronomical Institute, Graduate School of Science, Tohoku University, Aramaki, Aoba-ku, Sendai 980-8578, Japan*
[11]*European Southern Observatory, Karl-Schwarzschild-Strasse 2, D-85738 Garching, Germany*

ABSTRACT

We present the results of a narrow-band (H$_2$S1, $\lambda_c = 2.121\,\mu$m, $\delta\lambda = 0.021\,\mu$m) imaging search with Wide Field Camera/United Kingdom Infrared Telescope for Hα emitters (HAEs) around several potential signposts of rare ($\sim 10^{-7}$–10^{-8} comoving Mpc^{-3}) overdense regions at $z = 2.23$: an overdensity of quasi-stellar objects [QSOs; 2dF QSO Redshift Survey (2QZ) cluster], a powerful, high-redshift radio galaxy (HzRG) and a concentration of submillimetre galaxies (SMGs) and optically faint radio galaxies (OFRGs). In total, we detect 137 narrow-band emitter candidates down to emission-line fluxes of 0.5–1 $\times 10^{-16}$ erg s^{-1} cm^{-2}, across a total area of 0.56 deg^2 (2.1 $\times 10^5$ comoving Mpc^3 at $z = 2.23$) in these fields. The *BzK* colours of the emitters suggest that at least 80 per cent of our sample are likely to be HAEs at $z = 2.23$. This is one of the largest HAE samples known at $z \gtrsim 2$. Although there is no evidence for large-scale (20 comoving Mpc) overdensities of the emitters around the targets, we find modest ($\sim 3\sigma$) local overdensities associated with all three targets on smaller scales (5–10 comoving Mpc). In the 2QZ cluster field, the structure appears to be connecting the QSOs, while in the HzRG and SMG/OFRG fields, the structures are seen only in the vicinities of the targets. Our results suggest that these rare targets are located in local overdensities of galaxies, rather than average density regions, although it is not clear whether these structures are likely to evolve into rare, rich clusters. The *K*-band magnitudes and the Hα equivalent widths of the emitters are weakly correlated with the overdensities of the emitters: emitters in overdense regions are more evolved systems compared to those in underdense regions at $z = 2.23$. We find several examples of extended HAEs near to the targets, including a striking example with a spatial extent of 7.5 arcsec (60 kpc at $z = 2.23$) in the 2QZ cluster field, suggesting that these are relatively common in overdense regions. We conclude that narrow-band Hα surveys are efficient routes to map overdense regions at high redshifts and thus to understand the relation between the growth of galaxies and their surrounding large-scale structures.

Key words: galaxies: evolution – galaxies: formation – galaxies: high-redshift – cosmology: observations – early Universe.

1 INTRODUCTION

Some of the densest, large-scale galactic environments occur in galaxy clusters. These regions are characterized by populations of passive, early-type galaxies, whose properties contrast markedly with the star-forming, late-type galaxies found in the surrounding low-density field (e.g. Dressler 1980). The main formation phase of the stars in elliptical galaxies in clusters appears to have occurred at high redshift (probably $z \gtrsim 2$; e.g. Ellis et al. 1997; Blakeslee et al. 2003; Mei et al. 2009), in contrast to the field where most of the star formation activity occurs at $z \lesssim 2$ (e.g. Lilly et al. 1995; Thomas et al. 2005). Hence the evolution of galaxies in dense regions appears to be *accelerated* relative to that in low-density regions (e.g. Steidel et al. 2005; Tanaka et al. 2010; Tadaki et al. 2011; Hatch et al. 2011). As a result, while the average star formation rate (SFR) of a galaxy *decreases* with increasing local galaxy density in the low-redshift Universe (e.g. Lewis et al. 2002; Gómez et al. 2003; Patel et al. 2009, 2011), this trend should reverse at earlier times: with the SFR *increasing* with increasing galaxy density (Elbaz et al. 2007; Hayashi et al. 2010; Tran et al. 2010; Grützbauch et al. 2011). Hence the progenitors of these dense regions at high redshifts should be identifiable as overdensities of star-forming galaxies (Steidel et al. 1998, 2005; Venemans et al. 2007; Matsuda et al. 2009, 2010). If the growth of the galaxies is synchronized with that of their supermassive black holes, then populations of active galactic nuclei (AGN) should also be located in these overdense structures (Smail et al. 2003; Lehmer et al. 2009; Digby-North et al. 2010).

To identify the most massive high-redshift overdense regions, protoclusters, the most reliable, but time-consuming, technique is to find significant redshift overdensities in large spectroscopic redshift surveys of star-forming galaxies (Steidel et al. 1998, 2005; Chapman et al. 2009; Kurk et al. 2009). A quicker route is to perform such searches around luminous high-redshift sources, such as quasi-stellar objects (QSOs) or powerful high-redshift radio galaxies (HzRGs), where the expectation is that the massive black holes in these galaxies will be hosted by correspondingly massive galaxies which will signpost overdense regions at high redshifts. An even more efficient technique is to forego spectroscopy and instead search for concentrations of emission-line galaxies in narrow-band imaging surveys of these regions (e.g. Hu & McMahon 1996; Pascarelle et al. 1996; Keel et al. 1999; Kurk et al. 2000, 2004a,b; Kashikawa et al. 2007; Venemans et al. 2007; Hatch et al. 2011; Tanaka et al. 2011).

For target QSOs or HzRGs at $z > 2$, Lyα is redshifted into the optical and hence most of the narrow-band imaging surveys have targeted Lyα emission. However, Lyα is far from ideal as it is a resonance line and even a small amount of dust is enough to destroy the line, thus biasing searches against the dusty and perhaps most active galaxies in any structure. A better choice is to use Hα, which is less sensitive to dust and also a more accurate tracer of star formation (Kennicutt 1998; Garn et al. 2010). However, for galaxies at $z > 0.4$, Hα is redshifted into the near-infrared, and it is only through the recent development of panoramic, near-infrared imagers that narrow-band searches based on Hα have become possible (Geach et al. 2008, hereafter G08; Sobral et al. 2009a,b, 2010, 2011).

We have exploited the wide-field, near-infrared imaging capabilities of Wide Field Camera (WFCAM) on United Kingdom Infrared Telescope (UKIRT; Casali et al. 2007) to carry out an Hα imaging survey around several potential signposts of overdense regions at $z = 2.23$. The paper is structured as follows: Section 2 describes our target selection, while Section 3 details our observations and data reduction and Section 4 describes the results derived from these
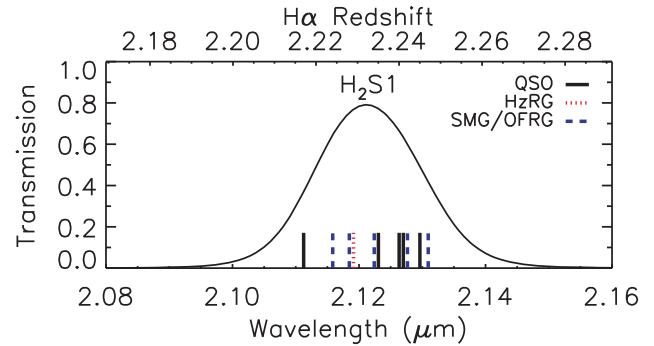

Figure 1. The transmission curve of the H$_2$S1 filter on UKIRT/WFCAM. We identify the wavelengths for Hα emission expected for the redshifts of our various targets: the QSOs in the 2QZ cluster, the HzRG (0200+015) and the SMG/OFRGs in SSA 13. The mean redshifts of the three sets of targets are clearly well matched to the transmission of the filter, allowing us to efficiently survey for HAEs in any associated structures.

data. Finally, Section 5 discusses our results and summarizes our main conclusions. We use Vega magnitudes unless otherwise stated and adopt cosmological parameters, $\Omega_M = 0.27$, $\Omega_\Lambda = 0.73$ and $H_0 = 73 \, \mathrm{km \, s^{-1} \, Mpc^{-1}}$. In this cosmology, the Universe at $z = 2.23$ is 2.9 Gyr old and 1.0 arcsec corresponds to a physical length of 8.1 kpc.

2 TARGET FIELD SELECTION

Our survey uses the H$_2$S1 narrow-band filter on WFCAM to isolate Hα emitters (HAEs) at $z = 2.23$. We plot the transmission curve of the narrow-band filter (H$_2$S1, $\lambda_c = 2.121 \, \mu m$, $\delta\lambda = 0.021 \, \mu m$) in Fig. 1. The redshift range of the Hα line corresponding to the 50 per cent transmission wavelengths of the filter is $z = 2.216$–2.248 (equivalent to a comoving length of 43.1 Mpc along the line of sight). We therefore searched for targets which could be potential signposts of overdense regions at $z \sim 2.23$ using the NASA/IPAC Extragalactic Database (NED).[1] We selected three targets: an overdensity of QSOs, a HzRG and a concentration of submillimetre galaxies (SMGs) and optically faint radio galaxies (OFRGs). We summarize the targets in Table 1.

2.1 2QZ cluster

Our first target is a concentration of QSOs selected from the 2dF QSO Redshift Survey (2QZ; Croom et al. 2001). There now appears to be some consensus that on average, overdensities of galaxies are present around typical QSOs (both radio-loud and radio-quiet) at $z < 2$ (e.g. Ellingson, Yee & Green 1991; Hall & Green 1998). However, using *overdensities* of QSOs should be a much clearer marker of structures at high redshifts (Clowes & Campusano 1991). We searched the whole equatorial region from the 2QZ for regions with more than four QSOs at $z = 2.216$–2.248 in a $1°$ diameter field. There are 285 QSOs at $z = 2.216$–2.248 in the 2QZ area of 289.6 deg^2 (or 1.1×10^8 comoving Mpc^3). We found only one structure satisfying the criteria in this volume indicating a number density of any associated structure of $\sim 10^{-8}$ comoving Mpc^{-3}. We refer to this target as the 2QZ cluster, it contains five QSOs at

---

[1] The NED is operated by the Jet Propulsion Laboratory, California Institute of Technology, under contract with the National Aeronautics and Space Administration.

Table 1. Summary of targets.

Field	Target	Redshift	Magnitude	Ref.[a]
2QZ cluster	2QZ J100351.5+001501	2.217	$B = 20.43$	1
	2QZ J100412.8+001257	2.240	$B = 18.57$	1, 2
	2QZ J100339.7+002109	2.241	$B = 19.58$	1, 2
	2QZ J100323.0+000725[b]	2.235	$B = 20.57$	1, 2
	2QZ J100204.0+001643[c]	2.245	$B = 20.42$	1, 2
0200+015	NVSS J020242+014910	2.229	$H = 19.26$	3, 4, 5, 6
SSA 13	SMM J131230.92+424051.0	2.247	$K = 19.29$	7
	SMM J131239.14+424155.7	2.242	$K = 19.49$	7
	RG J131207.74+423945.0	2.228	$K = 19.36$	8
	RG J131208.34+424144.4	2.234	$K = 19.10$	8
	RG J131236.05+424044.1	2.224	$K = 20.50$	8

[a]1 – Croom et al. (2004), 2 – Shen et al. (2007), 3 – Large et al. (1981), 4 – Röttgering et al. (1997), 5 – Condon et al. (1998), 6 – Iwamuro et al. (2003), 7 – Chapman et al. (2005), 8 – Smail et al. (2004).
[b]This source is just outside of the WFCAM field-of-view.
[c]This source is outside of the WFCAM field-of-view.

$z = 2.217$, 2.235, 2.240, 2.241 and 2.245 (see Fig. 1 and Table 1).[2] Four out of the five QSOs are even more strongly clustered in a 15×15 arcmin^2 region, with three of these QSOs falling within the field-of-view of a single WFCAM chip, with the fourth located just outside the field-of-view.

2.2 0200+015

Our second target is a HzRG: MRC 0200+015. The number density of HzRGs at $z = 2$–5 is a few times 10^{-8} comoving Mpc^{-3} (Miley & De Breuck 2008), and thus HzRGs are quite rare. There is growing evidence that a significant fraction of HzRGs reside in overdense environments (Kurk et al. 2000; Pentericci et al. 2000; Smail et al. 2003; Stevens et al. 2003; Miley et al. 2004; Kajisawa et al. 2006; Kodama et al. 2007; Venemans et al. 2007; Hatch et al. 2011; Tanaka et al. 2011). However, Best et al. (2003) show that HzRGs at $z \sim$ 1.5–2 are found in a very wide range of environments, from essentially no overdensity, through a small-scale central overdensity to larger scale overdensities. Using NED, we identified a HzRG, MRC 0200+015 (or NVSS J020242+014910) at $z = 2.229$ (hereafter 0200+015; Large et al. 1981; Röttgering et al. 1997; Condon et al. 1998). This HzRG field was observed using Hα imaging by van der Werf, Moorwood & Bremer (2000). They imaged an area of just 6.37 arcmin^2 down to a 3σ flux limit of 1.0×10^{-16} erg s^{-1} cm^{-2} for HAEs in redshift range of $z = 2.19$–2.26. Although they detected the HzRG as an HAE, they did not identify any additional HAE candidates around the HzRG. A single WFCAM chip has a field-of-view ~30 times larger than the area surveyed by van der Werf et al. (2000), giving us the first opportunity to conclusively search for a structure around this HzRG.

2.3 SSA 13

Our final target is a potential concentration of massive starburst galaxies. From redshift surveys of SMGs and OFRGs, a significant redshift spike was discovered at $z = 2.224$–2.247 ($\Delta z = 0.023$) in the Small Selected Area 13 (SSA 13) field (Smail et al. 2004; Chapman

[2] Four of the five QSOs are also listed in the Sloan Digital Sky Survey (SDSS) QSO catalogue (Shen et al. 2007).

et al. 2005). This spike contains two SMGs at $z = 2.242$ and 2.247 and three OFRGs at $z = 2.224$, 2.228 and 2.234 (see Fig. 1 and Table 1). This spike is one of the most prominent structures in their survey volume of a few times 10^6 comoving Mpc^3, suggesting a structure with a number density of a few times 10^{-7} comoving Mpc^{-3} (cf. Chapman et al. 2009).

3 OBSERVATIONS AND DATA REDUCTION

3.1 WFCAM observations

The three target fields were observed between 2006 May and 2010 April with WFCAM on UKIRT, using the K band and H$_2$S1 filters. We summarize the observations in Table 2. WFCAM has four 13.7×13.7 arcmin^2 chips offset by 20 arcmin (a comoving separation of 32 Mpc at $z = 2.23$). For our observations we place the target on one of the chips (chip 1 for the 2QZ cluster and SSA 13, chip 3 for 0200+015), with the other three chips providing control fields to derive the mean density of emitters ~40–60 comoving Mpc away from the target. To help with cosmic ray rejection over the relatively long narrow-band exposures (40–60 s), we used the non-destructive read (NDR) mode, whereas correlated double sampling (CDS) mode was used for the shorter broad-band exposures. To improve sampling of the point spread function (PSF) with the 0.4 arcsec pixels of WFCAM, the narrow-band frames were microstepped in a 2×2 grid with 1.2 arcsec offsets at each position, following a 14-point jitter sequence. The seeing in our observations varied between 0.7 and 1.2 arcsec full width at half-maximum (FWHM).

The data reduction was carried out in the same manner as for the HiZELS survey (G08; Sobral et al. 2009a,b, 2010, 2011). We flat-field a given image using a normalized median combination of the 13 remaining frames from the same sequence, taking care to mask-out bright sources in each frame. A world coordinate system is then automatically fit to each frame by querying the US Naval Observatory (USNO) A2.0 catalogue, on average returning ~100 sources to derive the astrometric fit. Frames are aligned and co-added with SWARP (Bertin et al. 2002). Both K band and H$_2$S1 magnitudes were calibrated by matching $K = 10$–15 stars from the Two Micron All Sky Survey (2MASS) All-Sky Catalog of Point Sources (Cutri et al. 2003) which are unsaturated in our frames. The magnitudes were not corrected for Galactic extinction, because the extinction is negligible in these bands ($\lesssim 0.01$ mag; Schlegel, Finkbeiner & Davis 1998).

The combined images were aligned and smoothed with Gaussian kernels to ensure that the final images in each field have the same seeing (0.9–1.2 arcsec FWHM). The size of each chip analysed here is 13.2×13.2 arcmin^2 after removal of low signal-to-noise ratio (S/N) regions near the edge. We also masked out haloes and cross-talk residuals of the bright stars ($K < 15$). The resultant total effective area of each chip is ~150–170 arcmin^2 (corresponding to a comoving volume of ~1.6–1.8×10^4 Mpc^3 for HAEs at $z = 2.23$ in the H$_2$S1 filter).

Source detection and photometry were performed using SEXTRACTOR version 2.5.0 (Bertin & Arnouts 1996). The source detections were made on the H$_2$S1 image. We detected sources with five connected pixels above 1.0–1.5σ of the sky noise. Each WFCAM chip has four amplifiers, we added small ($< \pm 0.1$ mag) shifts to the narrow-band zero-point magnitudes to make the median $K - NB$ colour zero for each region with the same amplifier in each chip. The magnitudes and colours are measured for each source in a 3 arcsec diameter aperture. In Table 2, we give the number densities of H$_2$S1 detected sources down to the 5σ limit in each field.

Table 2. Summary of observations and data.

Field	Coordinate (J2000) ($^h:^m:^s$) ($^\circ:':''$)	Date (mm/yyyy)	Filter	Chip	Exp time (ks)	Depth[a] (mag)	FWHM (arcsec)	Area (arcmin^2)	Number density[b] (arcmin^{-2})
2QZ cluster	10:03:51.0 +00:15:09	02/2010	H$_2$S1	1	34.44	19.9	0.9	169	8.1 (H$_2$S1 ≤ 19.9)
	10:05:37.2 +00:15:03			2	34.44	20.0	0.9	171	9.6 (H$_2$S1 ≤ 19.9)
	10:05:37.8 +00:41:22			3	34.44	19.9	0.9	172	10.1 (H$_2$S1 ≤ 19.9)
	10:03:51.5 +00:41:33			4	34.44	20.1	0.9	171	8.6 (H$_2$S1 ≤ 19.9)
	10:03:51.0 +00:15:09	02–03/2010	K	1	4.48	20.4	0.7	169	8.2 (K ≤ 19.9)
	10:05:37.2 +00:15:03			2	4.48	20.3	0.8	171	10.0 (K ≤ 19.9)
	10:05:37.8 +00:41:22			3	4.48	20.4	0.8	172	10.3 (K ≤ 19.9)
	10:03:51.5 +00:41:33			4	4.48	20.3	0.8	171	8.8 (K ≤ 19.9)
0200+015	02:02:42.6 +01:50:54	10/2007	H$_2$S1	3	13.44	19.6	0.9	148	8.3 (H$_2$S1 ≤ 19.5)
	02:00:56.0 +01:24:38			1	13.44	19.6	1.0	172	8.1 (H$_2$S1 ≤ 19.5)
	02:02:42.2 +01:24:35			2	13.44	19.7	1.1	169	7.2 (H$_2$S1 ≤ 19.5)
	02:00:56.1 +01:51:02			4	13.44	19.5	1.0	174	6.5 (H$_2$S1 ≤ 19.5)
	02:02:42.6 +01:50:54	10/2007	K	3	1.335	20.1	1.0	148	8.0 (K ≤ 19.5)
	02:00:56.0 +01:24:38			1	1.23	20.1	1.1	172	8.0 (K ≤ 19.5)
	02:02:42.2 +01:24:35			2	1.25	20.1	1.0	169	7.4 (K ≤ 19.5)
	02:00:56.1 +01:51:02			4	1.365	20.0	1.2	174	6.5 (K ≤ 19.5)
SSA 13	13:12:34.1 +42:40:43	05/2006	H$_2$S1	1	14.76	19.0	0.9	146	4.2 (H$_2$S1 ≤ 19.0)
	13:14:58.5 +42:40:49			2	14.32	19.1	0.9	174	5.1 (H$_2$S1 ≤ 19.0)
	13:14:58.2 +43:07:03			3	14.56	19.1	0.9	174	4.9 (H$_2$S1 ≤ 19.0)
	13:12:33.2 +43:07:08			4	14.96	19.1	0.9	171	4.6 (H$_2$S1 ≤ 19.0)
	13:12:34.1 +42:40:43	05/2006	K	1	0.625	19.7	1.0	147	4.3 (K ≤ 19.0)
	13:14:58.5 +42:40:49			2	0.615	19.7	0.9	174	5.0 (K ≤ 19.0)
	13:14:58.2 +43:07:03			3	0.63	19.8	0.9	174	4.8 (K ≤ 19.0)
	13:12:33.2 +43:07:08			4	0.62	19.5	0.9	171	4.7 (K ≤ 19.0)

[a]The 5σ limiting magnitude based on photometry with a 3 arcsec diameter aperture.
[b]The number density of H$_2$S1 detected sources.

We confirmed that these are consistent with K-band number counts of galaxies in UKIRT Infrared Deep Sky Survey (UKIDSS)/Deep Extragalactic Survey (DXS) by Kim et al. (2011). The number densities in each chip in each field agree within ±12 per cent, and the variations are also consistent with those seen in the UKIDSS/DXS data (Kim, private communication). The agreement suggests that our photometric calibration is reliable for each field.

3.2 Supporting observations

3.2.1 SCAM observations

To check contamination in our emitter sample from foreground and background line emitters, we obtained B- and z'-band images of the target fields with Subaru/Subaru Prime Focus Camera (Suprime-Cam; Miyazaki et al. 2002). We observed the 2QZ cluster field in 2009 November and the 0200+015 field in 2010 November. For the SSA 13 field, we used archival data. All the images were a single pointing of Suprime-Cam, covering only one chip of the WFCAM observations. The exposure times were 0.9–3.0 ks for the B band and 0.9–2.0 ks for z' band, respectively. The data were reduced using SDFRED (Yagi et al. 2002; Ouchi et al. 2004). For photometric calibration, we used the photometric standard stars in SA 101 and GD 71 fields (Landolt 1992; Smith et al. 2002) and SDSS z'-band images for the 2QZ cluster and SSA 13 fields. We corrected the magnitudes using the Galactic extinction map of Schlegel et al. (1998). The seeing (FWHM) of the stacked images are 0.9–1.2 arcsec for B band and 0.6–0.8 arcsec for z' band, respectively. The 1σ limiting AB magnitudes derived with 3 arcsec diameter aperture photometry are 27.0–27.6 ABmag for B band and 25.6–26.0 ABmag for z' band, respectively.

3.2.2 MOIRCS observations

The 0200+015 field was also observed with the K_s band and H$_2$S1 filters using Subaru/Multi-Object Infrared Camera and Spectrograph (MOIRCS; Suzuki et al. 2008) in 2007 August as part of engineering tests (performed by IT). The H$_2$S1 filter on MOIRCS has $\lambda_c = 2.116\,\mu m$ and $\delta\lambda = 0.021\,\mu m$. The H$\alpha$ redshift range covered with the H$_2$S1 filter is $z = 2.208–2.240$, which is only $\Delta z = 0.008$ smaller than that covered with the H$_2$S1 filter on WF-CAM. As one of the two chips had problems, we used only one chip. The exposure times were 1.17 ks for K_s band and 1.44 ks for H$_2$S1, respectively. We reduced the data using the MOIRCS imaging data reduction pipeline (MCSRED; Tanaka et al. 2011). For photometric calibration, we used the 2MASS All-Sky Catalogue of Point Sources (Cutri et al. 2003). The seeing (FWHM) of the stacked images are 0.48 arcsec for K_s band and 0.42 arcsec for H$_2$S1. The survey area is 12.4 arcmin^2 after masking low S/N regions. The 5σ limiting magnitudes calculated with a 0.84 arcsec diameter aperture are 22.3 mag for K_s band and 21.0 mag for H$_2$S1. The deeper, higher resolution images can be used as a test of the completeness of our WFCAM observations and to examine the Hα morphology in the central 4×3.5 arcmin^2 part of the 0200+015 field. These data will be discussed further in Tanaka et al. (in preparation).

3.2.3 LRIS observations

In addition, we carried out a long-slit spectroscopic observation of a bright emitter candidate in the 0200+015 field with Keck/Low Resolution Imaging Spectrometer (LRIS; Oke et al. 1995) in 2010 September. As the red-side CCD had problems, we used only the

blue arm. We used the 400/3400 grism and a 1.0-arcsec slit, yielding spectral coverage across ∼3500–5700 Å, at a spectral resolution of FWHM ∼ 7 Å or ∼600 km s^{-1}. The exposure time was 0.9 ks and we reduced the data with standard IRAF tasks. For wavelength calibration, we used arc lamp spectra with Hg, Cd and Zn lines, giving a wavelength calibration with an rms ∼0.6 Å. We also confirmed that there is no overall shift ($\lesssim$0.2 Å) for the wavelength calibration using the strong [O I] sky emission at 5577.3 Å.

4 ANALYSIS AND RESULTS

4.1 Selection of Hα emitter candidates

We show in Fig. 2 the colour–magnitude plots for the H_2S1-detected sample. From the H_2S1-detected sources with $H_2S1 \geq 5\sigma$ in each field, we select emitter candidates with the following criteria:

(1) $K - H_2S1 \geq 0.215$ (EW$_{obs} \geq 50$ Å),
(2) $\Sigma \geq 2.5$,

where Σ is the ratio between the H_2S1 excess and the uncertainty in the $K - H_2S1$ colour based on photometric errors of both K and H_2S1 for sources with a constant f_ν spectra. These criteria are the same as used in G08. One slight difference from G08 is that we

do not correct the K-band magnitudes using the $z' - K$ colour for the emitter selection, because we do not have z'-band images in our control fields. As we show below, this does not appear to adversely effect the purity of our narrow-band excess sample. We note that in each field, the limiting magnitudes between the chips are slightly different and so we use the shallowest 5σ limits and significance curves for the colour cut for both the targets and the surrounding control fields to ensure a fair comparison of the number densities in each field. The colour cuts correspond to flux limits of ∼0.5, ∼0.7 and ∼1.0 × 10^{-16} erg s^{-1} cm^{-2} for the 2QZ cluster, 0200+015 and SSA 13 fields, respectively.

In total we detect 137 emitter candidates over a combined area of 0.56 deg^2 (2.1 × 10^5 comoving Mpc^3 at $z = 2.23$) in the three fields. A flux limit of 0.5 × 10^{-16} erg s^{-1} cm^{-2} corresponds to a SFR (attenuation-uncorrected) of ∼14 M$_\odot$ yr^{-1} using the calibration of Kennicutt (1998). We listed the resulting catalogue of emitter candidates in the tables in Appendix A.

We have used the Suprime-Cam optical imaging to investigate the contamination from potential foreground and background line emitters (e.g. Paα emitters at $z = 0.13$, Paβ emitters at $z = 0.65$ and [O III] 5007 emitters at $z = 3.24$). We show in Fig. 3 the $B - z'$ and $z' - K$ colour–colour plot for emitter candidates in the target fields. This BzK colour–colour plane allows us to isolate $z \sim 1.4$–2.5

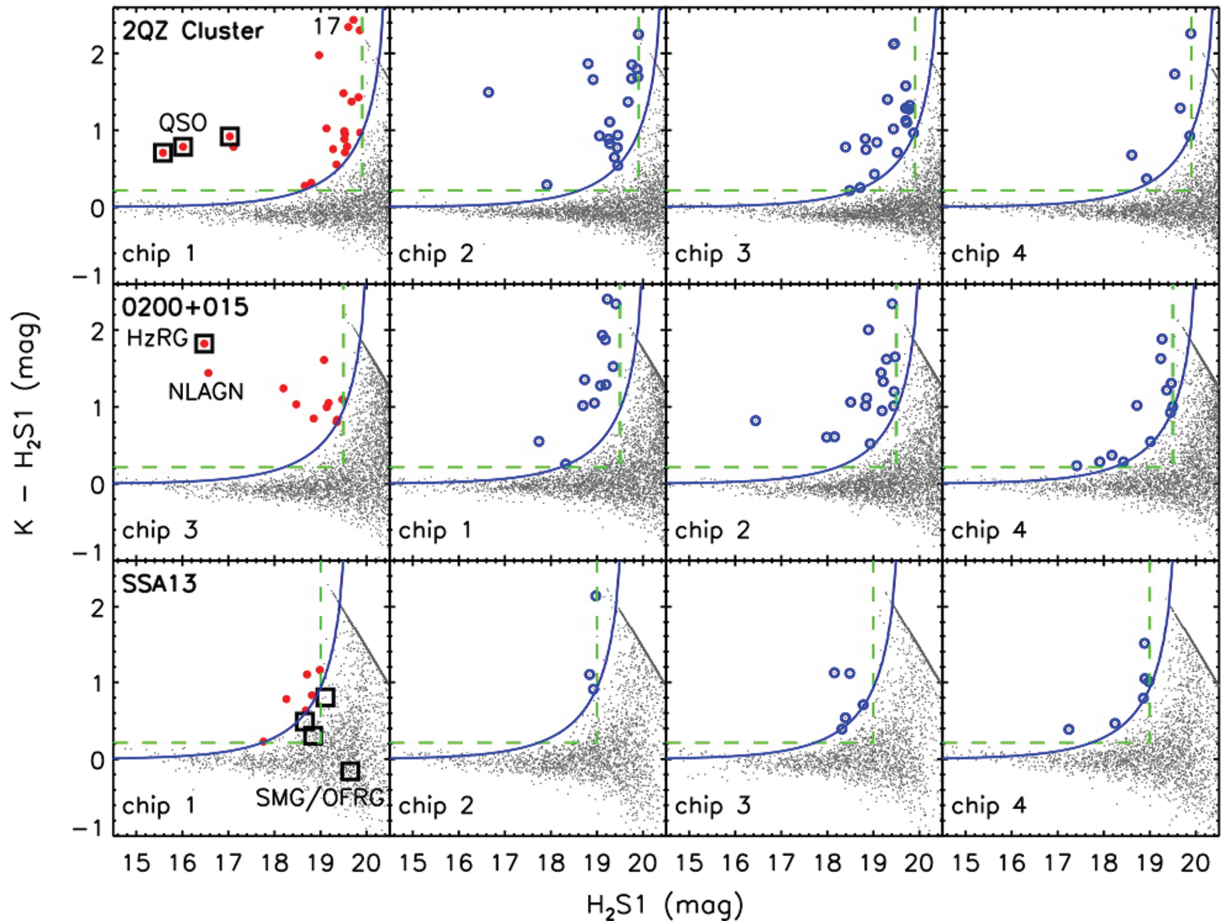**Figure 2.** Colour–magnitude plots showing H_2S1 versus $K - H_2S1$ for the H_2S1-detected sources in our three survey fields. The red filled and blue open circles identify the emitter candidates in the target and control fields, respectively (see Appendix A). The squares indicate the target QSOs, HzRG and SMG/OFRGs. The dashed lines are the colour cuts corresponding to $K - H_2S1 = 0.215$ (EW$_{obs} \geq 50$ Å) and $H_2S1 > 5\sigma$, used to select line emitters in our analysis. The solid curves show the expected 2.5σ error limit in the colour of a f_ν constant source. We also identify HAE17 surrounded by extended Hα nebula in the 2QZ cluster field, and the spectroscopically confirmed NLAGN at $z = 2.235$ in the 0200+015 field. All magnitudes and colours are measured with 3 arcsec diameter apertures. Comparison of the numbers of sources in the various fields suggests that no field has an overdensity of emitters on scales of a WFCAM chip.
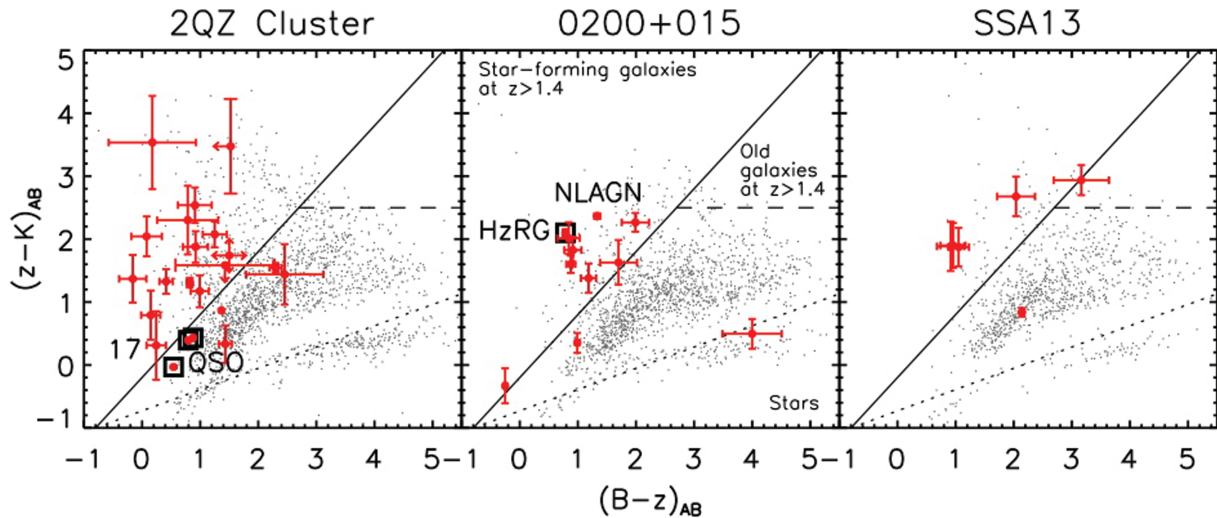
Figure 3. *BzK* diagram for emitter candidates in the *target* fields (i.e. the control fields are not included). At least 80 per cent of the emitter candidates satisfy the *BzK* criteria, $BzK \equiv (z - K)_{AB} - (B - z)_{AB} \geq -0.2$ or $(z - K)_{AB} > 2.5$ (Daddi et al. 2004), indicating that these are likely to be HAEs at $z = 2.23$. This plot suggests that the contamination rate from potential foreground and background line emitters in our emitter sample is $\lesssim 20$ per cent. The squares indicate the target QSOs, HzRG. We mark the HAE17 with an extended emission-line nebula in the 2QZ cluster field (left-hand panel). We also mark the spectroscopically confirmed NLAGN at $z = 2.235$ in the 0200+015 field (middle panel).

galaxies (Daddi et al. 2004), which are likely to be HAEs, from any foreground or background contamination (see G08). Although the *BzK* criteria, $BzK \equiv (z - K)_{AB} - (B - z)_{AB} \geq -0.2$ or $(z - K)_{AB} > 2.5$, were determined using a *BzK* filter set from different instruments, it has been confirmed that the same criteria can also be used for Suprime-Cam *B* and *z'*, and WFCAM *K* bands to select $z \sim 1.4$–2.5 galaxies (e.g. Hayashi et al. 2009). We find that $\gtrsim 80$ per cent of the emitter candidates satisfy the *BzK* criteria, indicating that these are likely to be $z \sim 2.23$ HAEs. Note that the three QSOs in the 2QZ cluster field are slightly outside the *BzK* colour-selection region ($BzK \sim 0.0$–0.2 mag), even though they are spectroscopically confirmed at $z \sim 2.23$. As the *BzK* analysis was designed for galaxies, and not for AGN, this is perhaps not surprising.

Without deep *U*-band data, it may be difficult to separate the [O III] 5007 emitters from the emitters, because the *BzK* colour cuts select galaxies at $z > 1.4$, but do not necessarily remove all galaxies with $z > 2.5$. For example, Hatch et al. (2011) showed that [O III] 5007 contamination rate for their emitters satisfying the *BzK* criteria is ~20 per cent using the *UBz* colours. However, their Hα surveys are six times deeper than our survey and thus it is possible that their emitters contain more background contamination. The depths of our survey are similar to (or 1–2 times deeper than) that of G08 and they showed that [O III] 5007 contamination rate is negligible for their emitters using the *Ugr* colours. Therefore [O III] 5007 contamination rate for our emitters may also be negligible.

The apparent contamination rate in our candidate emitter sample, ~20 per cent is similar to the ~10–20 per cent rates in other HAE surveys for overdense structures (Hatch et al. 2011; Tanaka et al. 2011). Although our contamination rate seems to be lower than the ~50–70 per cent rates in other HAE surveys in blank fields (G08; Hayes, Schaerer & Östlin 2010; Hatch et al. 2011), it is similar to the ~30 per cent rate for the subsample of Hayes et al.'s (2010) emitters with the similar flux range to our sample. As we show below, the resulting Hα luminosity functions of our emitters (in both target and control fields) and G08's HAEs are consistent, supporting the low contamination in our emitter sample. We note that for the following comparison of the number densities between the target and control fields, we have to use the full sample of emitter candidates (i.e.

before applying the *BzK* criteria) because we lack optical images in our control fields. However, due to our low contamination rate this only slightly affects the significance of the overdensities we find in these fields.

4.2 Properties of Hα emitter candidates

In Table 3, we summarize the number, number density and overdensity of the emitter candidates in each field. We derive the mean emitter density using the surrounding control fields for each target field. Our analysis of the number densities suggests that there is no significant excess of emitters in any of the three target fields on the scale of the WFCAM chips (21 comoving Mpc at $z = 2.23$). Note that in the 2QZ cluster field, the number of emitter candidates on

Table 3. Numbers, number densities and overdensities of emitter candidates on WFCAM chip scales.

Field	Chip	N	n (arcmin^{-2})	δ^a
2QZ cluster	1	22	0.13 ± 0.03	0.5 ± 0.4
Control	2, 3, 4	44	0.09 ± 0.01	0.0 ± 0.2
	2	18	0.11 ± 0.02	0.2 ± 0.3
	3	20	0.12 ± 0.03	0.4 ± 0.4
	4	6	0.04 ± 0.01	-0.6 ± 0.2
0200+015	3	11	0.07 ± 0.02	0.0 ± 0.3
Control	1, 2, 4	40	0.08 ± 0.01	0.0 ± 0.2
	1	12	0.07 ± 0.02	-0.1 ± 0.3
	2	16	0.09 ± 0.02	0.2 ± 0.4
	4	12	0.07 ± 0.02	-0.1 ± 0.3
SSA 13	1	6	0.04 ± 0.02	0.5 ± 0.7
Control	2, 3, 4	14	0.03 ± 0.01	0.0 ± 0.3
	2	3	0.02 ± 0.01	-0.4 ± 0.4
	3	5	0.03 ± 0.01	0.1 ± 0.6
	4	6	0.04 ± 0.01	0.3 ± 0.6

$^a \delta \equiv (n - \bar{n})/\bar{n}$, where $\bar{n}$ is the mean density of emitter candidates derived from the three control fields surrounding each target field.
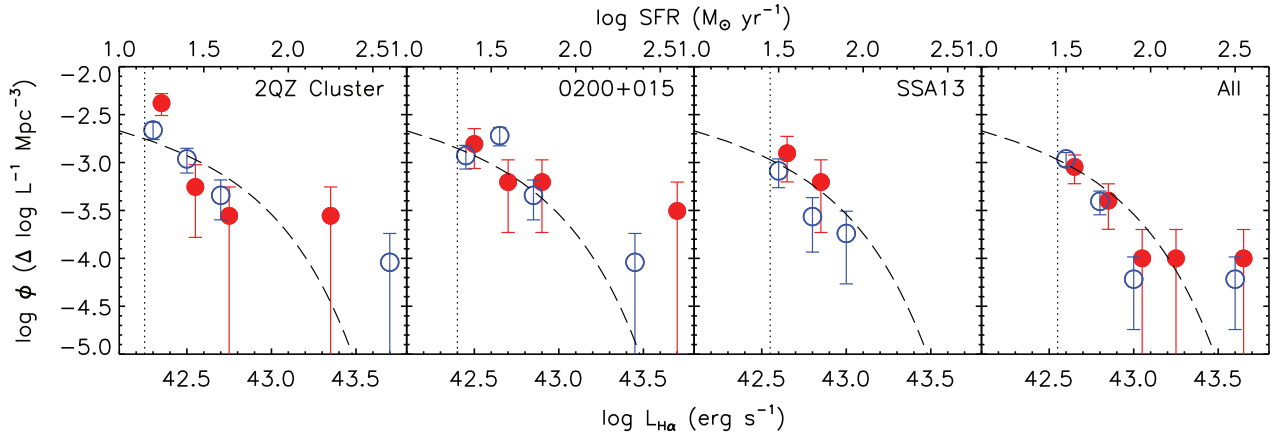
Figure 4. The Hα LFs in the target and control fields. The LFs in the target (filled symbol) and control fields (open symbol) appear to be consistent with that of the blank field. We exclude the QSOs and HzRG from the emitter sample to derive the LF. As the contamination rate is $\lesssim 20$ per cent in our emitter sample in the target fields, we assume all the emitter candidates are HAEs in this plot. The dashed line shows the blank field Hα luminosity function at $z = 2.23$ from G08. The dotted lines represent the detection limits of our emitter sample. The data points in the control fields are slightly shifted (-0.05 dex) for display purposes.

chip 4 appears to be lower than on the other chips. However, we have confirmed that across all fields the total number of all H$_2$S1-detected sources (not just those showing excess emission in the H$_2$S1 filter) on chip 4 is not different with those in the other chips, as shown in Table 2. Thus, the lower number of the emitter candidates on chip 4 in the 2QZ cluster field is likely to be real (i.e. a void of emitters).

We compare the Hα luminosity functions (LFs) of the emitter candidates in the target and control fields in Fig. 4. All the LFs appear to be consistent with the blank field LF of $z = 2.23$ HAEs from G08. We could not find any clear difference between the shapes of LFs in the target and control fields. In this comparison, we have excluded the three QSOs and HzRG from our emitter sample.

To search for overdensities on scales smaller than the chip field-of-view, we show the sky distributions and smoothed density maps of emitter candidates in these fields in Figs 5–7. The surface density maps are generated with a Gaussian smoothing kernel with a size chosen to match the median distance between the nearest-neighbour emitters in the control fields, $\sigma = 1.4$ arcmin for the 2QZ cluster and 0200+015, and $\sigma = 2.3$ arcmin for SSA 13. In these maps, we can see modest overdensities ($\sim 3\sigma$ deviations from the average densities) of emitters within all three target fields. In the 2QZ cluster field, the structure appears to be connecting the QSOs, while in the HzRG and SMG/OFRG fields, the structures appear to be smaller and only seen in the vicinities of the targets. We discuss these structures below, but we first note that the estimated significance of these overdensities may be conservative, because the potential contamination will be unclustered and so should slightly decrease the significance of any real overdensities, although again we stress that the contamination rate in our emitter sample is expected to be quite low (~ 20 per cent) so this should not be a large effect.

2QZ cluster. As can be seen in Fig. 5, the overdensity in the 2QZ cluster field comprises a structure apparently connecting the QSOs at $z = 2.23$. This structure contains a 2.9σ density peak from the average density derived in the control fields, and it is the second highest peak in the full density map of the 2QZ cluster and the surrounding three control fields. The peak density of this structure is 3.7 times higher than the average density. The three target QSOs lie in weak overdense regions ($\delta \sim 1$) rather than the local density peak. The highest density peak is located in the west edge of the

chip 2. Near to the highest density peak, there is a very bright, point-source emitter, which may be another luminous AGN at $z = 2.23$ as the emission-line luminosity is similar to the target QSOs. In the chip 3, there is a filamentary structure extending over at least 20 comoving Mpc from the south-west to the north-east. Although we lack data between the chips, these structures seen in the chips 2 and 3 may be parts of a single large-scale structure associated with the 2QZ cluster,[3] extending over 60 comoving Mpc (cf. Steidel et al. 1998; Hayashino et al. 2004; Matsuda et al. 2005).

0200+015. There is a local overdensity of emitters in the vicinity of the HzRG, with a 3.0σ deviation from the average density. The local emitter density of this peak is 3.3 times higher than the average density. This is one of the highest density peaks in the 0200+015 and the surrounding control fields (see Fig. 6). We confirmed that all of the five emitter candidates in this overdensity satisfy the BzK criteria indicating that they are highly likely to be HAEs at $z = 2.23$. Four out of the five HAEs in the overdensity, including the HzRG, are also observed with our independent MOIRCS data and selected as narrow-band excess sources, supporting the reliability of our sample selection. Finally, we obtained optical spectroscopy of the 0200-C3-HAE2, the second brightest HAE in the 0200+015 field, using LRIS on Keck. The 0200-C3-HAE2 is a member of the overdensity and 1.8 arcmin (900 kpc at $z = 2.23$ in projection) away from the HzRG. The spectrum confirms that this galaxy is at $z = 2.235$. We present the spectrum of this source in Fig. 8, which shows strong Lyα, C IV 1549 and He II 1640 emission lines with velocity widths of FWHM ~ 1000 km s^{-1}, suggesting that this HAE is in fact a narrow-line AGN (NLAGN) and further confirms that our emitter selection works well to identify HAE at $z = 2.23$.

SSA 13. We also find a hint for a local overdensity of emitters in the SSA 13 field. The local overdensity in the vicinity of the

---

[3] If there is a galaxy overdensity between the chips, a signature might appear as associated absorption lines in the spectrum of background QSOs (e.g. Young, Sargent & Boksenberg 1982; Chen, Lanzetta & Webb 2001; Wilman et al. 2007; Crighton et al. 2011). There is one background SDSS QSO at $z = 3.045$ (SDSS J100428+001825.6; Shen et al. 2007). However, we could not see any clear Lyα absorption line nor C IV absorption between $z = 2.216$ and 2.245 in its spectrum.
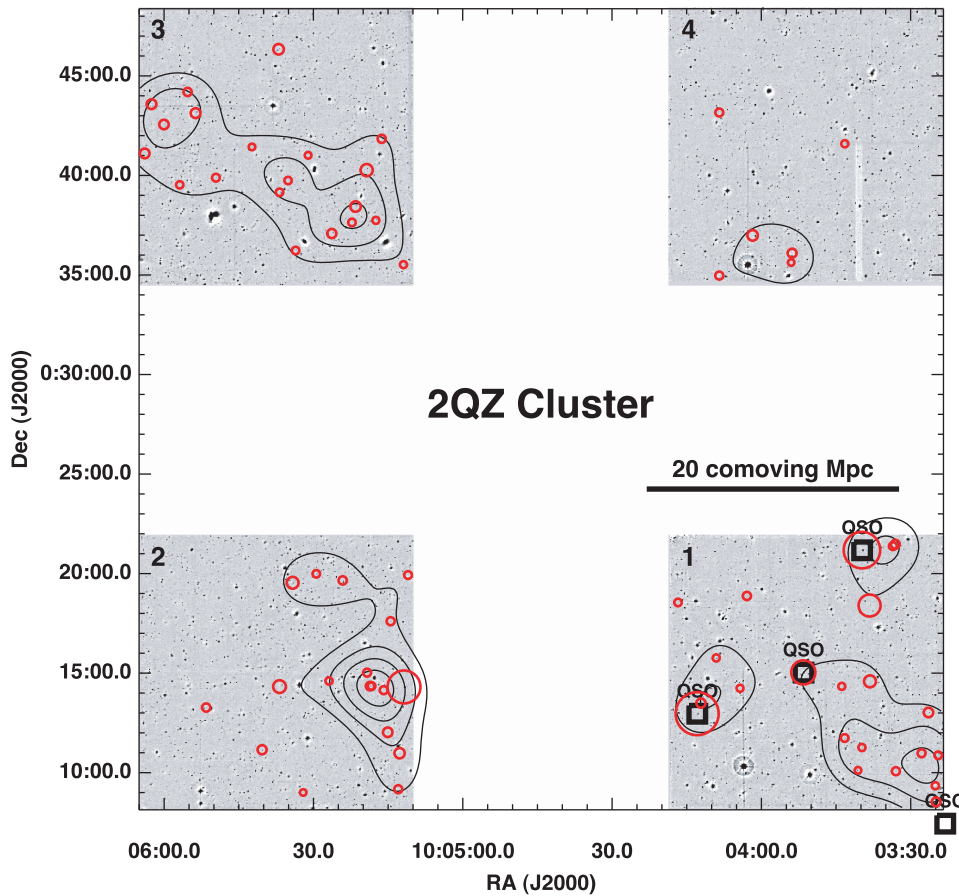
Figure 5. The sky distribution and smoothed density map of emitter candidates at $z \sim 2.23$ in the 2QZ cluster field overlaid on the WFCAM H$_2$S1 images. In the target field (chip 1), we see a structure which appears to connect up the QSOs at $z = 2.23$ in this region. In the control fields, chip 2 contains a overdense region with a new $z = 2.23$ QSO candidate and chip 3 shows a filamentary structure. The contours show deviations of local emitter densities from the average density of the control fields (chips 2, 3 and 4), from 0.5σ with 1σ intervals. The squares indicate the positions of the QSOs. The red circles indicate the emitter candidates and the size is proportional to the emission-line flux.

SMG/OFRG concentration has a 2.9σ deviation from the average density. The local emitter density of this peak is 2.7 times higher than the average density. This is the highest density peak in the SSA 13 and surrounding control fields (see Fig. 7). All the SMGs and OFRGs are detected in the K band and their K-band magnitudes are consistent with the previous results from Smail et al. (2004). However, none of them is selected as emitter candidates, although we detect four out of the five SMGs or OFRGs in our H$_2$S1 image (see Fig. 2). This may be due to the relatively shallow depth of the H$_2$S1 image in SSA 13 (Table 2). For two of the OFRGs in this field the observed Hα equivalent widths have been spectroscopically measured to be EW$_{obs}$ = 65 and 80 Å (Swinbank et al. 2004). However, a source with $K \gtrsim 19$ needs to exhibit a narrow-band excess of $K - H_2$S1 $\gtrsim 1$ or EW$_{obs} \geq 400$ Å to comply with our emitter selection criteria. The Hα of the undetected SMG at $z = 2.247$ falls near the edge of the H$_2$S1 transmission curve (see Fig. 1).

We examine the emission-line morphology of the emitter candidates with $\Sigma \geq 4$ (Fig. 9). The magnitudes and isophotal areas are measured in the continuum-corrected H$_2$S1 images with isophotes determined with $\sim 2\sigma$ surface brightness thresholds of 1.0, 1.4 and 2.3×10^{-17} erg s^{-1} cm^{-2} arcsec^{-2} for the 2QZ cluster, 0200+015 and SSA 13 fields, respectively. While the isophotal areas of most of the emitter candidates are similar to, or somewhat larger than, the sequence of the point sources, several emitters in the 2QZ cluster

and 0200+015 fields show significantly larger isophotal areas than expected for point sources.

The giant HAE candidate in the 2QZ cluster field, referred to as 2QZC-C1-HAE17 in Table A1, has a spatial extent of ~ 7.5 arcsec (60 kpc at $z = 2.23$) in our narrow-band image. This HAE is only 34 arcsec (~ 300 kpc) from the brightest target QSO (2QZ J100412.8+001257 or 2QZC-C1-HAE1) in this region (see Fig. 10) and the continuum source associated with HAE17 satisfies the BzK criteria, suggesting that this is likely to be an Hα emission-line nebula at $z = 2.23$. The emission-line nebula has a continuum-corrected H$_2$S1 magnitude of 19.0 mag in an isophotal aperture with an area of 9.4 arcsec^2, corresponding to an emission-line flux of 1.7×10^{-16} erg s^{-1} cm^{-2} or an Hα luminosity of 6×10^{42} erg s^{-1}. There is no evidence for an optically bright AGN in HAE17 as the continuum source is spatially resolved in the B- and z'-band images and in addition the HAE does not have any bright radio source with $f_{1.4\,\mathrm{GHz}} \geq 1$ mJy in the Very Large Array (VLA) Faint Images of the Radio Sky at Twenty-cm (FIRST) catalogue (Becker, White & Helfand 1995), suggesting that it is not similar to the extended emission-line nebulae often seen around powerful radio galaxies (e.g. McCarthy 1993), such as 0200+015 (Fig. 9). Unfortunately there is no deep X-ray data in this field necessary to further constrain the presence of an obscured AGN in this nebula.
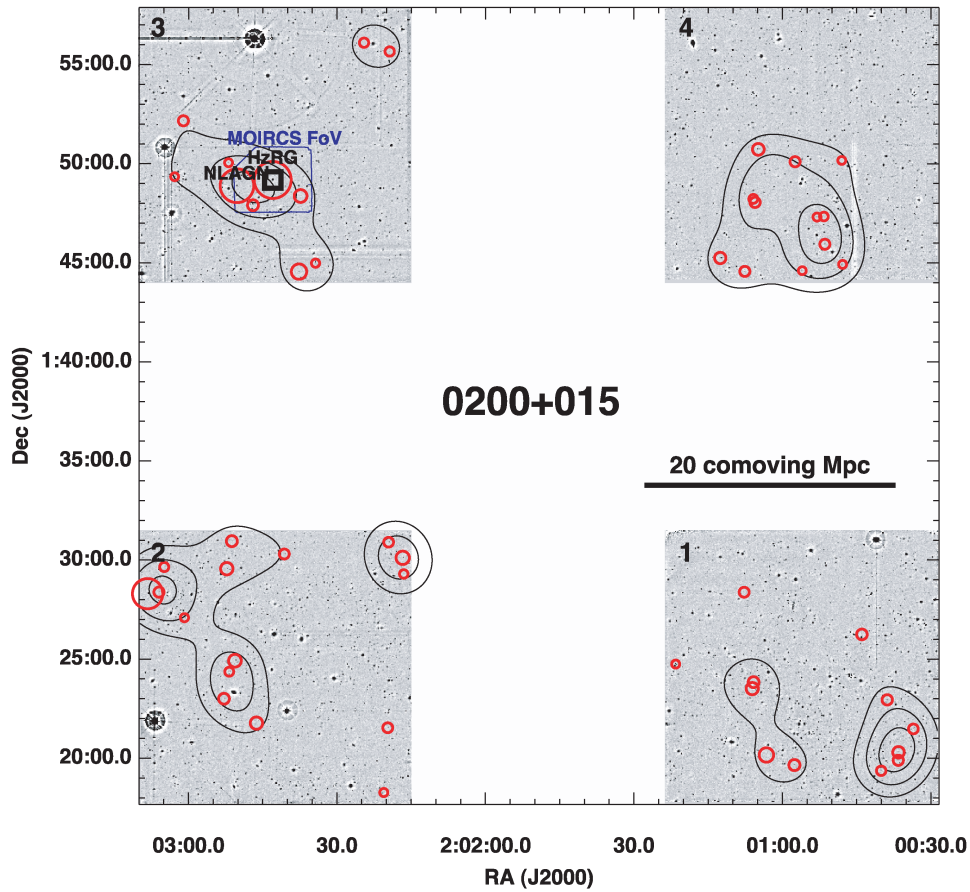
Figure 6. The sky distribution and smoothed density map of emitter candidates at $z \sim 2.23$ in the 0200+015 field. In the target field (chip 3), we see an overdensity centred on the HzRG. The region surrounded by the blue line is the area surveyed with MOIRCS. Our MOIRCS observations confirm the reality of the four narrow-band excesses sources in this region. The contours show deviations of local emitter densities from the average density of the control fields (chips 1, 2 and 4), from 0.5σ with 1σ intervals. The square indicates the position of the HzRG. The red circles indicate the emitter candidates and the size is proportional to the emission-line flux.

As shown by Fig. 9 there are several potentially resolved emitters in the 0200+015 field: 0200-C3-HAE1 (HzRG), HAE2 (NLAGN), HAE3 and HAE4. All show evidence of having larger isophotal areas than expected for point sources with their narrow-band magnitudes. To investigate the morphologies of these HAEs we can make use of the high-quality imaging from MOIRCS in this field. In Fig. 11 we show thumbnails of the three resolved HAEs from MOIRCS, as well as a fourth more compact HAE which falls in the image: 0200-C3-HAE6. This figure clearly demonstrates the presence of bright Hα emission-line nebulae around the HzRG and NLAGN, with spatial extents of 4–5 arcsec corresponding to ~30–40 kpc at $z = 2.23$, while 0200-C3-HAE4 also exhibits fainter but similarly extended emission-line nebulosity. The K-band morphology of HAE4 also seems extended on 3 arcsec or ~25 kpc scales, with the Hα emission line peaking on the outer edge of the K-band structure. These properties of the HAE4 may resemble to galaxies with large discs at $z = 1.4$–3 (Labbé et al. 2003). These extended HAEs, along with HAE17 in the 2QZ cluster field, are obviously relatively common and indicate that star formation is occurring over large regions, comparable to the size of massive galaxies at the present day, even at $z = 2.23$. Current surveys of the HAEs in lower density regions at this epoch have turned up few such examples (e.g. Fig. 9 and G08) and so it is possible that these extended

emission-line nebulae are an environmental signature, as has been found for extended Lyα nebulae (Lyα blobs; e.g. Steidel et al. 2000; Matsuda et al. 2004, 2009; Palunas et al. 2004; Prescott et al. 2008; Yang et al. 2010).

We can also use the MOIRCS imaging to determine the efficiency of fibre spectrograph surveys of HAEs using instruments such as Fibre Multi-Object Spectrograph (FMOS) on Subaru (Kimura et al. 2010). In Fig. 12, we therefore show the growth curves of the emission-line fluxes from two examples of extended and compact HAEs (0200-C3-HAE4 and HAE6) as a function of photometric aperture using the MOIRCS continuum corrected H_2S1 image. For comparison, we also plot a PSF using a bright star in the MOIRCS H_2S1 image. This result suggests that the ~10–40 per cent of the total fluxes are missing in the 3 arcsec diameter aperture used in this work, while ~40–80 per cent could be missed if we measured the flux in a 1.2 arcsec diameter aperture fibre similar to Subaru/FMOS. This suggests that care must be taken to assess the fibre losses for such spectroscopic surveys, even of high-redshift galaxies, as a fraction of the targets may exhibit highly extended emission. However, as Fig. 12 demonstrates, in these cases aperture corrections using rest-frame ultraviolet (UV) continuum images could be employed to correct these losses and should all the recovery of ~80–100 per cent of the total fluxes.
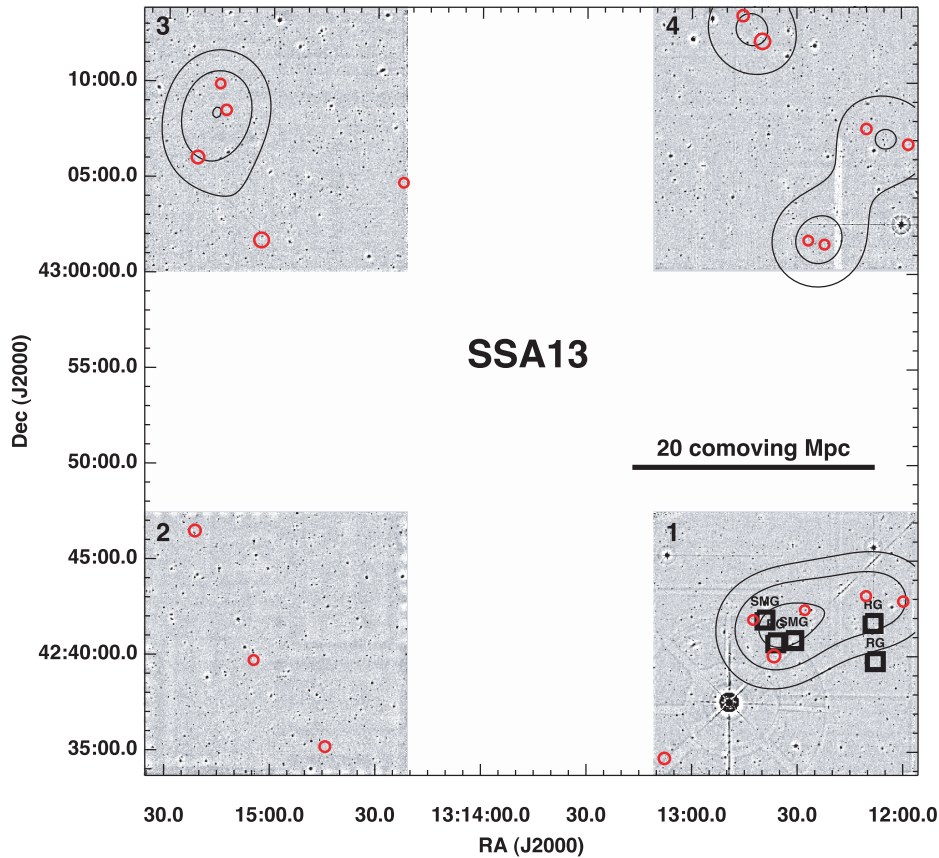
Figure 7. The sky distribution and smoothed density map of emitter candidates at $z \sim 2.23$ in the SSA 13 field. In the target field (chip 1), we see a modest overdensity near to the SMG/OFRG structure. The contours show deviations of local emitter densities from the average density of the control fields (chips 2, 3 and 4), from 0.5σ with 1σ intervals. The squares indicate the positions of the SMGs and OFRGs. The red circles indicate the emitter candidates and the size is proportional to the emission-line flux.
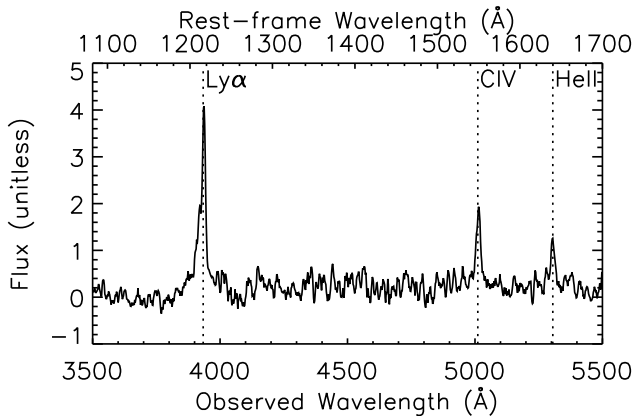

Figure 8. The one-dimensional optical spectrum of the second brightest HAE (0200-C3-HAE2) in the 0200+015 field. We see strong emission lines corresponding to Lyα, C IV 1549 and He II 1640 which yield a redshift of $z = 2.235$, confirming this as an Hα-selected source. The strength of He II and the velocity widths of FWHM ~ 1000 km s^{-1} for these lines indicate that this HAE is a NLAGN. This spectroscopic result confirms that our emitter selection works well to identify HAE at $z = 2.23$.

Finally, in Fig. 13 we plot the observed K-band magnitudes and equivalent widths of the emitters as a function of the emitter local overdensities (the local densities around each emitters are calculated excluding the source itself). In order to select an homogeneous emitter sample from the three fields, given their different depths, we exclude emitter candidates in the 2QZ cluster and 0200+015 fields below the detection limit in the SSA 13 field ($F_{H\alpha} < 1 \times 10^{-16}$ erg s^{-1} cm^{-2}). From this combined sample, we also exclude potential AGN with emission-line fluxes similar to those of target QSOs and HzRG ($F_{H\alpha} > 7 \times 10^{-16}$ erg s^{-1} cm^{-2}), this then means we can crudely relate the K-band magnitude to a measure of the stellar mass of the galaxies, assuming that all the HAEs have roughly comparable mass-to-light ratios. We therefore use the relation estimated from G08, $\log_{10} M_* \sim -0.4K(\text{mag}) + 18.45$, to convert our K-band magnitudes into stellar masses. In a similar manner, as the Hα luminosity is a good indicator of SFR (Kennicutt 1998), we can use our Hα equivalent widths for the HAEs to estimate their specific star formation rates (SSFRs). We show both of these inferred properties in Fig. 13. We see that both the K-band magnitudes and equivalent widths (or stellar masses and SSFRs) of the resulting sample show weak correlations with the local overdensities. The Spearman's rank correlation coefficients are $r_s = -0.21$ (K-band magnitude) and -0.27 (equivalent width), respectively, indicating that the sample distributions are consistent with random distributions at 8 per cent (K-band magnitude) and 3 per cent (equivalent width) confidence levels. Thus our observations suggest there is weak evidence that the emitters in overdense regions tend to have smaller SSFR compared to those in underdense regions, potentially indicating accelerated evolution in the build-up of galaxies in overdense regions at $z = 2.23$ (cf. Steidel et al. 2005; Tanaka et al. 2010; Hatch et al. 2011).
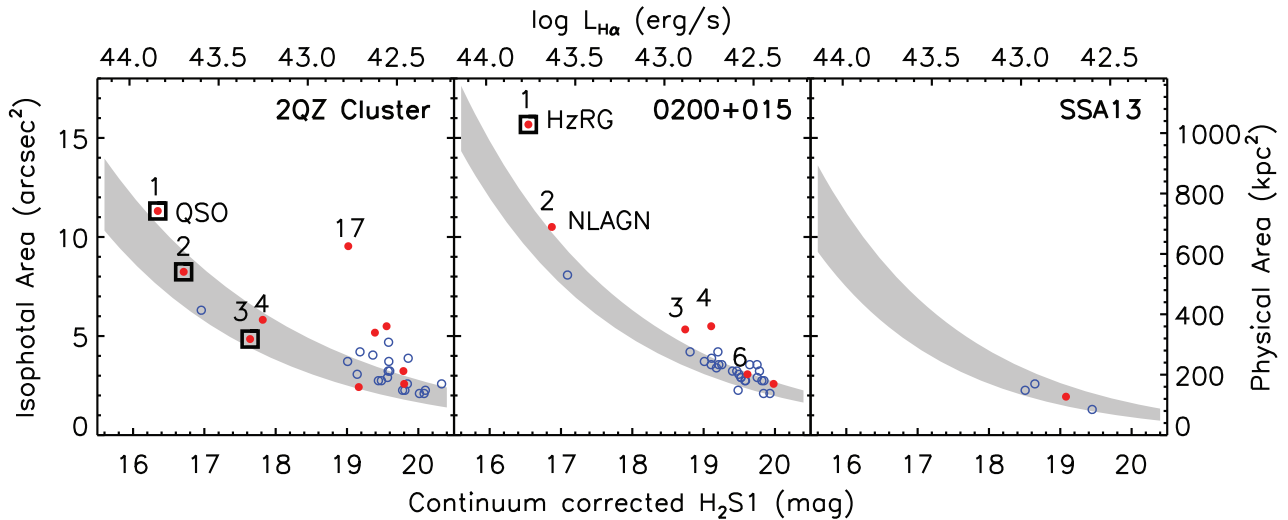
Figure 9. The continuum-corrected H$_2$S1 magnitudes versus the continuum-corrected H$_2$S1 isophotal areas for emitter candidates with $\Sigma \geq 4$. The grey-scale bands represent the point source tracks *without* narrow-band excess, while the red filled circles indicate those emitters lying on the same chip as the target in each field and the blue open circles are the emitters in the surrounding control fields. In addition, we highlight the target QSOs and HzRG and label other sources using the naming scheme from Tables A1 and A2. The isophotal areas of the point sources show a characteristic variation with magnitudes and so we can conclude those narrow-band excess sources significantly above this envelope are well resolved. In particular, HAE17 in the 2QZ cluster field shows an isophotal area some three times larger than the locus of point sources in the same magnitude range indicating it is very extended. The magnitudes and areas are measured with isophotes determined with ∼2σ surface brightness thresholds of 1.0, 1.4 and 2.3 × 10^{-17} erg s^{-1} cm^{-2} arcsec^{-2} for the 2QZ cluster, 0200+015 and SSA 13 fields, respectively.
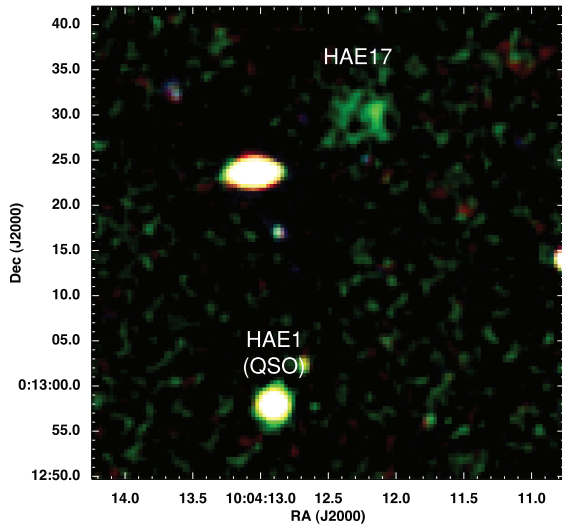

Figure 10. False colour image (blue for SCAM z', green for H$_2$S1 and red for K) of the brightest QSO, 2QZC-C1-HAE1 (2QZ J100412.8+001257) and the extended HAE candidate, 2QZC-C1-HAE17, in the 2QZ cluster field. The angular separation between the HAE1 and HAE17 is 34 arcsec (∼300 kpc in projection). The HAE17 appears to have an extended emission-line nebula with a spatial extent of ∼7.5 arcsec (∼60 kpc at $z = 2.23$) and an Hα luminosity of 6 × 10^{42} erg s^{-1}.

5 DISCUSSION AND CONCLUSIONS

We have undertaken a narrow-band imaging survey of three target fields which contain potential signposts of rare overdense regions with space densities of ∼10^{-7}–10^{-8} comoving Mpc^{-3} and local control fields to assess the significance of any overdensities. Our survey detects 137 emitter candidates in a volume of 2.1 × 10^5 comoving Mpc^3 at $z = 2.23$ down to limiting Hα fluxes of ∼0.5–1 × 10^{-16} erg s^{-1} cm^{-2} (equivalent to attenuation-uncorrected SFR
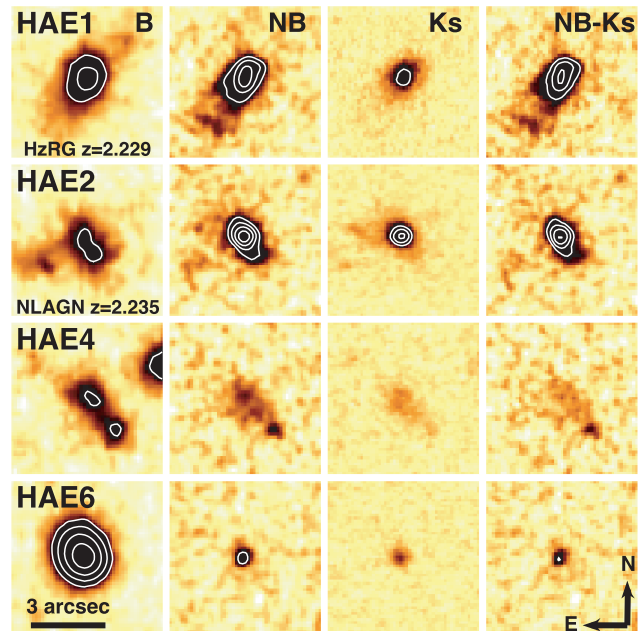
Figure 11. Subaru/Suprime-Cam (B) and MOIRCS (H$_2$S1, K_s and H$_2$S1−K_s) thumbnail images of the HAEs in the overdensity around the HzRG in the 0200+015 field. The size of the images is 5 × 5 arcsec^2 (∼40 × 40 kpc^2). The seeing sizes of the images are FWHM = 1.0 arcsec (Suprime-Cam) and 0.5 arcsec (MOIRCS), respectively. All the four emitter satisfy the *BzK* criteria, indicating that 0200-C3-HAE4 and HAE6 are also likely to be at $z \sim 2.23$. We see that 0200-C3-HAE1, 2 and 4 exhibit extended Hα emission on scales of ∼3–5 arcsec (or 25–40 kpc), while 0200-C3-HAE6 appears to be compact. The same magnitude range is used to display for the MOIRCS images. The contours show the bright peaks.

Figure 12. Growth curves of the emission-line fluxes of two typical extended and compact HAEs with MOIRCS imaging in the 0200+015 field. The solid curves show fractions of covered fluxes of two representative HAEs: 0200-C3-HAE4 (extended), 0200-C3-HAE6 (compact), and a PSF corresponding to the 0.5 arcsec seeing MOIRCS Hα images. The dashed curves show the fractions of the rest-frame UV continuum in the 1.0 arcsec SCAM *B*-band images. The total fluxes are measured with a 5 arcsec diameter aperture and normalized to unity. The dashed vertical lin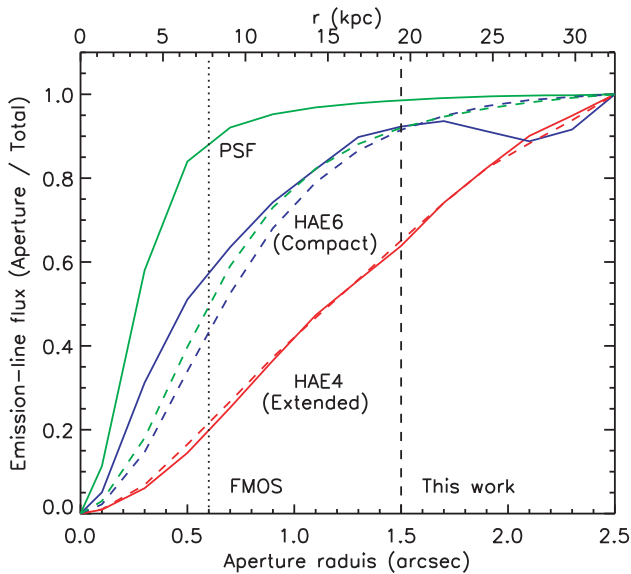e indicates the 3 arcsec diameter aperture photometry used in this work. The dotted vertical line shows the 1.2 arcsec diameter of fibre of Subaru/FMOS (Kimura et al. 2010). This suggests that the FMOS fibre may miss up to ~40–80 per cent of the total emission-line fluxes from HAEs at $z \sim 2$. However, aperture corrections based on the rest-frame UV continuum images should be able to recover most of the fluxes within 20 per cent uncertainty levels.

of $\gtrsim 14$–$28\,M_\odot\,yr^{-1}$). This is one of the largest HAE samples currently available at $z \gtrsim 2$. Based on supporting optical imaging of these fields, we estimate that at least 80 per cent of these narrow-band excess sources likely correspond to HAEs at $z = 2.23$. We have confirmed the reliability of our sample selection in one field, 0200+015, by using independent H$_2$S1 observations from MOIRCS/Subaru, recovering all four HAEs selected in the overlap area from our WFCAM imaging, and also spectroscopically confirmed that one of the bright emitters in this field is an Hα source at $z = 2.235$.

Wide-field narrow-band Hα survey is one of the most effective routes to map overdense regions of star-forming galaxies at high redshifts. Our analysis of the density distribution of emitters in our survey, using statistical corrections for the blank-field density (including any potential foreground or background contamination) derived from the parallel control fields, indicates the presence of 3σ local (5–10 comoving Mpc scale) overdensities in all three of our target fields. There are also six similar local density peaks with $\geq 2.5\sigma$ in the control fields (nine WFCAM chips). In the blank-field survey of G08 (HiZELS), four out of the 12 WFCAM chips contain $\geq 2.5\sigma$ local overdensity peaks. If we use this frequency in the blank field, the probabilities that three out of three WFCAM chips (the target fields) and at least six out of nine WFCAM chips (the control fields) contain the $\geq 2.5\sigma$ local overdensity peaks are calculated to be only 3.7 and 4.0 per cent, respectively. Thus the overdense regions found in the target and surrounding control fields are likely to be associated with the targets with 96 per cent confidence levels. Therefore, we conclude that the targets are located in local overdensities of galaxies, rather than average regions. However, there is no clear evidence for large-scale overdensities around the targets on the WFCAM chip scale (20 comoving Mpc), and therefore it is not clear whether these local overdense regions around the targets will evolve into rare, rich clusters at the present day. In the 2QZ cluster
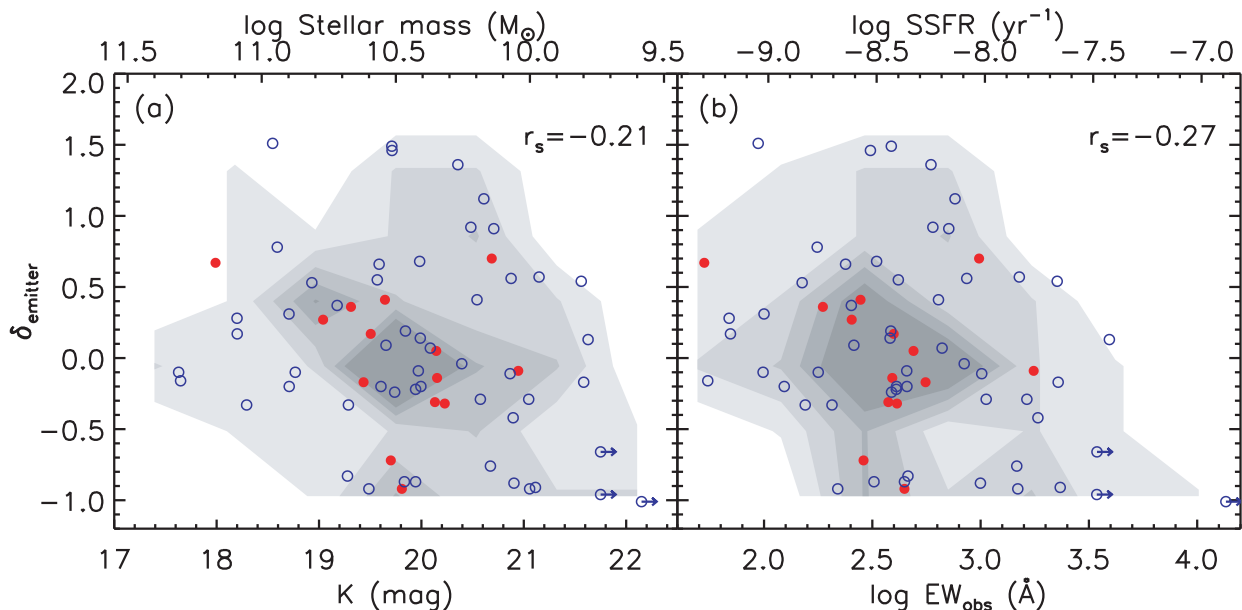
Figure 13. The local overdensities versus the observed *K*-band magnitudes (a) and equivalent widths (b) of emitter candidates with Hα luminosities of $L_{H\alpha} = 0.35$–$2 \times 10^{43}\,erg\,s^{-1}$. Both of the *K*-band magnitudes and equivalent widths show weak correlations with the local overdensities of emitters. At $z = 2.23$, star-forming galaxies in overdense environments seem to have brighter *K*-band magnitudes, and thus possibly higher masses, compared to those in underdense environments. The red filled circles indicate those emitters lying on the same chip as the target in each field, while the blue open circles are the emitters in the surrounding control fields. The shaded regions highlight the number densities of the distributions of emitters. We label each panel with Spearman's rank correlation coefficient for the distribution, r_s, indicating the presence of weak correlations in both these plots.

field, the structure connecting the target QSOs has an overdensity of $\delta \sim 3$, while the overdensities in the vicinities of the QSOs are not large ($\delta \sim 1$). These properties may be similar to the large-scale structure found around another QSO cluster at $z = 1.1$ (Tanaka et al. 2000, 2001). In the HzRG and SMG/OFRG fields, there are local overdense regions in the vicinities of the targets, with overdensities of $\delta \sim 2$. Our survey is $\sim$15–25 times wider, but $\sim$5–10 times shallower than previous Hα protocluster surveys around HzRGs at $z \gtrsim 2$ (e.g. Kurk et al. 2004a; Hatch et al. 2011). Future deeper H_2S1 imaging observations will more accurately reveal the true overdensities of these structures.

Narrow-band Hα survey is also useful to understand the relation between the growth of galaxies and their surrounding large-scale structures. We could not find any clear difference between the Hα luminosity functions in the target and surrounding control (or blank) fields. However, analysing our sample of emitters and their environments, we find that their K-band magnitudes and equivalent widths (crudely corresponding to stellar masses and SSFRs) show weak correlations with the local overdensities of emitters. These results hint at the possibility that the emitters in overdense region may be more evolved systems compared to those in underdense regions. This would be consistent with the picture that star formation activity is accelerated (or enhanced) in galaxies in overdense regions at $z \gtrsim 2$. Similar results have also been reported from the previous searches for protoclusters at $z \gtrsim 2$ (Steidel et al. 2005; Tanaka et al. 2010; Hatch et al. 2011).

Deep narrow-band imaging also enables us to examine the Hα morphology of emitters, which provides us with information on star formation activity in high-redshift galaxies during their formation phase and/or on their surrounding circum galactic medium. In the 0200+015 field, our deeper, higher resolution MOIRCS narrow-band imaging confirms that the Hα emission from three HAEs (including both the HzRG and the newly discovered NLAGN) is significantly extended on scales of 25–40 kpc. We find several examples of such extended HAEs in our target fields, including a striking example in the 2QZ cluster field, suggesting that these are relatively common in high-density regions, with no clear examples in our control fields or reported in the field survey of G08. The spatial extent of these systems, $\sim$30–60 kpc, suggests that star formation at $z = 2.23$ is occurring over regions in these galaxies comparable to the size of the largest galaxies at the present day or large-scale gas outflows are interacting with the surrounding circum galactic medium in overdense environments. Looking at the Hα luminosity of the most extended example, 6×10^{42} erg s^{-1} for HAE17 in the 2QZ cluster field, if we assume Lyα/Hα = 8.75 (case B and no dust extinction; e.g. McCarthy, Elston & Eisenhardt 1992), then its Lyα luminosity is expected to be 5×10^{43} erg s^{-1}, which would make its spatial extent and Lyα luminosity comparable to those of giant Lyα blobs (e.g. Matsuda et al. 2011). However, we need spectroscopic follow-up or deeper Hα imaging to confirm that this extended emission-line nebula is real and is the first Hα blob. More generally, future higher resolution Hα imaging and integral field spectroscopic observations are essential to investigate the star formation activity and gas dynamics and metallicity of the interstellar medium in these spatially extended emitters to constrain their role in galaxy formation.

ACKNOWLEDGMENTS

REFERENCES

Becker R. H., White R. L., Helfand D. J., 1995, ApJ, 450, 559
Bertin E., Arnouts S., 1996, A&A, 117, 393
Bertin E., Mellier Y., Radovich M., Missonnier G., Didelon P., Morin B., 2002, in Bohlender D. A., Durand D., Handley T. H., eds, ASP Conf. Ser. Vol. 281, Astronomical Data Analysis Software and Systems XI. Astron. Soc. Pac., San Francisco, p. 228
Best P. N., Lehnert M. D., Miley G. K., Röttgering H. J. A., 2003, MNRAS, 343, 1
Blakeslee J. P. et al., 2003, ApJ, 596, L143
Casali M. et al., 2007, A&A, 467, 777
Chapman S. C., Blain A. W., Smail I., Ivison R. J., 2005, ApJ, 622, 772
Chapman S. C., Blain A., Ibata R., Ivison R. J., Smail I., Morrison G., 2009, ApJ, 691, 560
Chen H.-W., Lanzetta K. M., Webb J. K., 2001, ApJ, 556, 158
Clowes R. G., Campusano L. E., 1991, MNRAS, 249, 218
Condon J. J., Cotton W. D., Greisen E. W., Yin Q. F., Perley R. A., Taylor G. B., Broderick J. J., 1998, AJ, 115, 1693
Crighton N. H. M. et al., 2011, MNRAS, 414, 28
Croom S. M., Smith R. J., Boyle B. J., Shanks T., Loaring N. S., Miller L., Lewis I. J., 2001, MNRAS, 322, L29
Croom S. M., Smith R. J., Boyle B. J., Shanks T., Miller L., Outram P. J., Loaring N. S., 2004, MNRAS, 349, 1397
Cutri R. M. et al., 2003, The IRSA 2MASS All-Sky Point Source Catalog, NASA/IPAC Infrared Science Archive. http://irsa.ipac.caltech.edu/applications/Gator/
Daddi E., Cimatti A., Renzini A., Fontana A., Mignoli M., Pozzetti L., Tozzi P., Zamorani G., 2004, ApJ, 617, 746
Digby-North J. A. et al., 2010, MNRAS, 407, 846
Dressler A., 1980, ApJ, 236, 351
Elbaz D. et al., 2007, A&A, 468, 33
Ellingson E., Yee H. K. C., Green R. F., 1991, ApJ, 371, 49
Ellis R. S., Smail I., Dressler A., Couch W. J., Oemler A., Jr, Butcher H., Sharples R. M., 1997, ApJ, 483, 582
Garn T. et al., 2010, MNRAS, 402, 2017
Geach J. E., Smail I., Best P. N., Kurk J., Casali M., Ivison R. J., Coppin K., 2008, MNRAS, 388, 1473 (G08)
Gómez P. L. et al., 2003, ApJ, 584, 210
Grützbauch R., Chuter R. W., Conselice C. J., Bauer A. E., Bluck A. F. L., Buitrago F., Mortlock A., 2011, MNRAS, 412, 2361
Hall P. B., Green R. F., 1998, ApJ, 507, 558
Hatch N. A., Kurk J. D., Pentericci L., Venemans B. P., Kuiper E., Miley G. K., Röttgering H. J. A., 2011, preprint (arXiv:1103.4364)
Hayashi M. et al., 2009, ApJ, 691, 140
Hayashi M., Kodama T., Koyama Y., Tanaka I., Shimasaku K., Okamura S., 2010, MNRAS, 402, 1980
Hayashino T. et al., 2004, AJ, 128, 2073
Hayes M., Schaerer D., Östlin G., 2010, A&A, 509, L5
Hu E. M., McMahon R. G., 1996, Nat, 382, 231
Iwamuro F. et al., 2003, ApJ, 598, 178
Kajisawa M., Kodama T., Tanaka I., Yamada T., Bower R., 2006, MNRAS, 371, 577

Kashikawa N., Kitayama T., Doi M., Misawa T., Komiyama Y., Ota K., 2007, ApJ, 663, 765

Keel W. C., Cohen S. H., Windhorst R. A., Waddington I., 1999, AJ, 118, 2547

Kennicutt R. C., Jr, 1998, ARA&A, 36, 189

Kim J.-W., Edge A. C., Wake D. A., Stott J. P., 2011, MNRAS, 410, 241

Kimura M. et al., 2010, PASJ, 62, 1135

Kodama T., Tanaka I., Kajisawa M., Kurk J., Venemans B., De Breuck C., Vernet J., Lidman C., 2007, MNRAS, 377, 1717

Kurk J. D. et al., 2000, A&A, 358, L1

Kurk J. D., Pentericci L., Röttgering H. J. A., Miley G. K., 2004a, A&A, 428, 793

Kurk J. D., Pentericci L., Overzier R. A., Röttgering H. J. A., Miley G. K., 2004b, A&A, 428, 817

Kurk J. et al., 2009, A&A, 504, 331

Labbé I. et al., 2003, ApJ, 591, L95

Landolt A. U., 1992, AJ, 104, 340

Large M. I., Mills B. Y., Little A. G., Crawford D. F., Sutton J. M., 1981, MNRAS, 194, 693

Lehmer B. D. et al., 2009, ApJ, 691, 687

Lewis I. et al., 2002, MNRAS, 334, 673

Lilly S. J., Tresse L., Hammer F., Crampton D., Le Fevre O., 1995, ApJ, 455, 108

McCarthy P. J., 1993, ARA&A, 31, 639

McCarthy P. J., Elston R., Eisenhardt P., 1992, ApJ, 387, L29

Matsuda Y. et al., 2004, AJ, 128, 569

Matsuda Y. et al., 2005, ApJ, 634, L125

Matsuda Y. et al., 2009, MNRAS, 400, L66

Matsuda Y. et al., 2010, MNRAS, 403, L54

Matsuda Y. et al., 2011, MNRAS, 410, L13

Mei S. et al., 2009, ApJ, 690, 42

Miley G., De Breuck C., 2008, A&AR, 15, 67

Miley G. K. et al., 2004, Nat, 427, 47

Miyazaki S. et al., 2002, PASJ, 54, 833

Oke J. B. et al., 1995, PASP, 107, 375

Ouchi M. et al., 2004, ApJ, 611, 660

Palunas P., Teplitz H. I., Francis P. J., Williger G. M., Woodgate B. E., 2004, ApJ, 602, 545

Pascarelle S. M., Windhorst R. A., Keel W. C., Odewahn S. C., 1996, Nat, 383, 45

Patel S. G., Holden B. P., Kelson D. D., Illingworth G. D., Franx M., 2009, ApJ, 705, L67

Patel S. G., Kelson D. D., Holden B. P., Franx M., Illingworth G. D., 2011, ApJ, 735, 53

Pentericci L. et al., 2000, A&A, 361, L25

Prescott M. K. M., Kashikawa N., Dey A., Matsuda Y., 2008, ApJ, 678, L77

Röttgering H. J. A., van Ojik R., Miley G. K., Chambers K. C., van Breugel W. J. M., de Koff S., 1997, A&A, 326, 505

Schlegel D. J., Finkbeiner D. P., Davis M., 1998, ApJ, 500, 525

Shen Y. et al., 2007, AJ, 133, 2222

Smail I., Scharf C. A., Ivison R. J., Stevens J. A., Bower R. G., Dunlop J. S., 2003, ApJ, 599, 86

Smail I., Chapman S. C., Blain A. W., Ivison R. J., 2004, ApJ, 616, 71

Smith J. A. et al., 2002, AJ, 123, 2121

Sobral D. et al., 2009a, MNRAS, 398, 75

Sobral D. et al., 2009b, MNRAS, 398, L68

Sobral D., Best P. N., Geach J. E., Smail I., Cirasuolo M., Garn T., Dalton G. B., Kurk J., 2010, MNRAS, 404, 1551

Sobral D., Best P. N., Smail I., Geach J. E., Cirasuolo M., Garn T., Dalton G. B., 2011, MNRAS, 411, 675

Steidel C. C., Adelberger K. L., Dickinson M., Giavalisco M., Pettini M., Kellogg M., 1998, ApJ, 492, 428

Steidel C. C., Adelberger K. L., Shapley A. E., Pettini M., Dickinson M., Giavalisco M., 2000, ApJ, 532, 170

Steidel C. C., Adelberger K. L., Shapley A. E., Erb D. K., Reddy N. A., Pettini M., 2005, ApJ, 626, 44

Steidel C. C., Bogosavljević M., Shapley A. E., Kollmeier J. A., Reddy N. A., Erb D. K., Pettini M., 2011, preprint (arXiv:1101.2204)

Stevens J. A. et al., 2003, Nat, 425, 264

Suzuki R. et al., 2008, PASJ, 60, 1347

Swinbank A. M., Smail I., Chapman S. C., Blain A. W., Ivison R. J., Keel W. C., 2004, ApJ, 617, 64

Tadaki K.-I., Kodama T., Koyama Y., Hayashi M., Tanaka I., Tokoku C., 2011, PASJ, 63, 437

Tanaka I., Yamada T., Aragón-Salamanca A., Kodama T., Miyaji T., Ohta K., Arimoto N., 2000, ApJ, 528, 123

Tanaka I., Yamada T., Turner E. L., Suto Y., 2001, ApJ, 547, 521

Tanaka M., De Breuck C., Venemans B., Kurk J., 2010, A&A, 518, A18

Tanaka I. et al., 2011, PASJ, 63, 415

Thomas D., Maraston C., Bender R., Mendes de Oliveira C., 2005, ApJ, 621, 673

Tran K.-V. H. et al., 2010, ApJ, 719, L126

van der Werf P. P., Moorwood A. F. M., Bremer M. N., 2000, A&A, 362, 509

Venemans B. P. et al., 2007, A&A, 461, 823

Wilman R. J., Morris S. L., Jannuzi B. T., Davé R., Shone A. M., 2007, MNRAS, 375, 735

Yagi M., Kashikawa N., Sekiguchi M., Doi M., Yasuda N., Shimasaku K., Okamura S., 2002, AJ, 123, 66

Yang Y., Zabludoff A., Eisenstein D., Davé R., 2010, ApJ, 719, 1654

Young P., Sargent W. L. W., Boksenberg A., 1982, ApJS, 48, 455

APPENDIX A: TABLES AND THUMBNAIL IMAGES OF Hα EMITTER CANDIDATES

Table A1. Properties of the emitter candidates in the 2QZ cluster (C1) and the control fields (C2, C3 and C4).

ID	Coordinate (J2000) (^{h}:^{m}:^{s}) ($^\circ$:$'$:$''$)	H$_2$S1 (mag)	K (mag)	Σ	EW$_{obs}$ (Å)	$\log F^a_{H\alpha}$ (cgs)	$\log L^b_{H\alpha}$ (cgs)	SFR$^c_{H\alpha}$	M^d_*	Note
2QZC-C1-HAE1	10:04:12.90 +00:12:57.9	15.58	16.29	110.0	219	−14.68	43.88	606	11.9	QSO
2QZC-C1-HAE2	10:03:39.79 +00:21:10.8	16.02	16.80	79.1	255	−14.82	43.74	436	11.7	QSO
2QZC-C1-HAE3	10:03:51.58 +00:15:02.1	17.03	17.95	34.5	327	−15.18	43.38	190	11.3	QSO
2QZC-C1-HAE4	10:03:38.27 +00:18:23.8	17.11	17.89	28.8	255	−15.26	43.30	159	11.3	...
2QZC-C1-HAE5	10:03:25.05 +00:09:20.5	18.66	18.93	3.0	66	−16.24	42.33	17	10.9	...
2QZC-C1-HAE6	10:04:09.08 +00:15:45.9	18.80	19.12	3.0	78	−16.24	42.32	17	10.8	*BzK*
2QZC-C1-HAE7	10:03:38.19 +00:14:35.2	18.97	20.95	8.5	1758	−15.79	42.77	47	10.1	*BzK*
2QZC-C1-HAE8	10:03:26.43 +00:13:01.2	19.13	20.15	5.3	391	−15.99	42.57	29	10.4	*BzK*
2QZC-C1-HAE9	10:03:32.97 +00:10:04.5	19.27	20.03	3.8	241	−16.13	42.43	21	10.4	*BzK*
2QZC-C1-HAE10	10:04:04.29 +00:14:14.4	19.34	19.90	2.9	156	−16.26	42.30	16	10.5	*BzK*

Table A1 – *continued*

ID	Coordinate (J2000) (^{h}:^{m}:^{s}) ($^{\circ}$:$'$:$''$)	H2S1 (mag)	K (mag)	Σ	EW_{obs} (Å)	$\log F^a_{H\alpha}$ (cgs)	$\log L^b_{H\alpha}$ (cgs)	$SFR^c_{H\alpha}$	M^d_*	Note
2QZC-C1-HAE11	10:03:33.09 +00:21:28.4	19.50	20.98	4.6	808	−16.05	42.51	26	10.1	*BzK*
2QZC-C1-HAE12	10:03:33.57 +00:21:22.8	19.52	20.50	3.7	369	−16.16	42.41	20	10.2	*BzK*
2QZC-C1-HAE13	10:03:24.48 +00:10:52.4	19.52	20.40	3.4	307	−16.19	42.38	19	10.3	*BzK*
2QZC-C1-HAE14	10:03:43.28 +00:11:44.5	19.53	20.48	3.5	344	−16.17	42.39	19	10.3	*BzK*
2QZC-C1-HAE15	10:03:43.84 +00:14:20.2	19.53	20.24	2.9	221	−16.26	42.31	16	10.4	*BzK*
2QZC-C1-HAE16	10:03:39.78 +00:11:15.8	19.57	20.36	3.0	257	−16.24	42.32	16	10.3	*BzK*
2QZC-C1-HAE17	10:04:12.16 +00:13:29.7	19.60	21.95	5.0	3460	−16.02	42.54	28	9.7	*BzK*
2QZC-C1-HAE18	10:03:27.82 +00:10:58.6	19.67	21.04	3.8	682	−16.14	42.42	21	10.0	*BzK*
2QZC-C1-HAE19	10:03:24.89 +00:08:31.8	19.71	>22.15	>4.6	>4237	−16.06	42.50	25	<9.6	...
2QZC-C1-HAE20	10:04:16.74 +00:18:33.0	19.82	21.25	3.4	745	−16.19	42.37	19	9.9	...
2QZC-C1-HAE21	10:04:02.90 +00:18:52.5	19.85	>22.15	>4.0	>3167	−16.12	42.44	22	<9.6	...
2QZC-C1-HAE22	10:03:40.59 +00:10:07.1	19.86	20.83	2.6	356	−16.30	42.26	14	10.1	...
2QZC-C2-HAE1	10:05:11.82 +00:14:18.3	16.65	18.14	64.3	824	−14.91	43.65	354	11.2	...
2QZC-C2-HAE2	10:05:12.69 +00:10:58.7	17.91	18.20	6.3	70	−15.92	42.64	35	11.2	...
2QZC-C2-HAE3	10:05:36.81 +00:14:19.4	18.81	20.67	9.6	1469	−15.73	42.83	53	10.2	...
2QZC-C2-HAE4	10:05:34.17 +00:19:32.4	18.92	20.58	8.3	1061	−15.80	42.76	46	10.2	...
2QZC-C2-HAE5	10:05:15.08 +00:12:01.8	19.06	19.98	5.4	331	−15.99	42.57	30	10.5	...
2QZC-C2-HAE6	10:05:18.63 +00:14:20.9	19.25	20.14	4.3	308	−16.08	42.48	24	10.4	...
2QZC-C2-HAE7	10:05:40.32 +00:11:09.1	19.27	20.38	4.9	450	−16.03	42.53	27	10.3	...
2QZC-C2-HAE8	10:05:24.12 +00:19:39.4	19.28	20.10	4.1	276	−16.11	42.45	22	10.4	...
2QZC-C2-HAE9	10:05:26.89 +00:14:36.4	19.38	20.02	3.1	193	−16.22	42.34	17	10.4	...
2QZC-C2-HAE10	10:05:29.41 +00:19:59.4	19.44	20.21	3.3	250	−16.19	42.37	18	10.4	...
2QZC-C2-HAE11	10:05:15.88 +00:14:08.7	19.45	20.39	3.7	337	−16.15	42.42	21	10.3	...
2QZC-C2-HAE12	10:05:32.07 +00:09:00.4	19.45	20.00	2.5	151	−16.31	42.25	14	10.5	...
2QZC-C2-HAE13	10:05:12.95 +00:09:10.2	19.68	21.05	3.8	680	−16.14	42.42	21	10.0	...
2QZC-C2-HAE14	10:05:14.51 +00:17:36.5	19.75	21.43	3.9	1084	−16.13	42.43	21	9.9	...
2QZC-C2-HAE15	10:05:51.55 +00:13:16.4	19.76	21.61	4.0	1436	−16.12	42.45	22	9.8	...
2QZC-C2-HAE16	10:05:10.98 +00:19:55.6	19.87	21.66	3.6	1312	−16.17	42.40	20	9.8	...
2QZC-C2-HAE17	10:05:18.32 +00:14:21.0	19.89	21.59	3.4	1125	−16.18	42.38	19	9.8	...
2QZC-C2-HAE18	10:05:19.23 +00:15:01.5	19.90	>22.15	>3.8	>2862	−16.14	42.42	21	<9.6	...
2QZC-C3-HAE1	10:05:19.28 +00:40:16.0	18.40	19.18	8.8	253	−15.77	42.79	49	10.8	...
2QZC-C3-HAE2	10:05:17.44 +00:37:44.5	18.48	18.70	2.9	50	−16.26	42.30	16	11.0	...
2QZC-C3-HAE3	10:05:31.07 +00:41:00.7	18.71	18.96	2.7	60	−16.29	42.27	15	10.9	...
2QZC-C3-HAE4	10:05:21.53 +00:38:26.3	18.82	19.71	6.5	310	−15.91	42.65	36	10.6	...
2QZC-C3-HAE5	10:05:53.65 +00:43:07.9	18.84	19.59	5.7	238	−15.96	42.60	31	10.6	...
2QZC-C3-HAE6	10:05:56.86 +00:39:31.8	19.02	19.45	3.1	112	−16.22	42.34	17	10.7	...
2QZC-C3-HAE7	10:05:26.30 +00:37:05.0	19.07	19.92	5.0	285	−16.02	42.54	27	10.5	...
2QZC-C3-HAE8	10:06:00.01 +00:42:33.6	19.31	20.71	5.4	713	−15.99	42.57	30	10.2	...
2QZC-C3-HAE9	10:05:36.99 +00:46:20.2	19.35	>22.15	>6.6	>13565	−15.90	42.66	36	<9.6	...
2QZC-C3-HAE10	10:05:55.27 +00:44:11.7	19.43	20.45	4.0	387	−16.12	42.45	22	10.3	...
2QZC-C3-HAE11	10:06:02.53 +00:43:34.8	19.44	21.56	5.6	2257	−15.97	42.59	31	9.8	...
2QZC-C3-HAE12	10:06:03.90 +00:41:06.3	19.46	21.59	5.5	2281	−15.97	42.59	31	9.8	...
2QZC-C3-HAE13	10:05:11.91 +00:35:31.2	19.52	20.23	2.9	221	−16.25	42.31	16	10.4	...
2QZC-C3-HAE14	10:05:49.59 +00:39:53.2	19.70	20.99	3.6	599	−16.16	42.40	20	10.1	...
2QZC-C3-HAE15	10:05:16.28 +00:41:50.4	19.70	21.28	3.9	934	−16.12	42.44	22	9.9	...
2QZC-C3-HAE16	10:05:33.56 +00:36:13.9	19.70	20.83	3.3	463	−16.20	42.36	18	10.1	...
2QZC-C3-HAE17	10:05:35.09 +00:39:44.7	19.72	20.82	3.2	444	−16.21	42.35	18	10.1	...
2QZC-C3-HAE18	10:05:36.78 +00:39:09.2	19.77	21.04	3.3	587	−16.19	42.37	18	10.0	...
2QZC-C3-HAE19	10:05:22.24 +00:37:38.4	19.79	21.11	3.3	634	−16.19	42.37	18	10.0	...
2QZC-C3-HAE20	10:05:42.34 +00:41:26.0	19.87	20.84	2.6	353	−16.30	42.26	14	10.1	...
2QZC-C4-HAE1	10:04:01.76 +00:36:59.4	18.61	19.29	6.6	206	−15.90	42.66	36	10.7	...
2QZC-C4-HAE2	10:03:43.23 +00:41:35.6	18.93	19.30	3.0	93	−16.24	42.32	17	10.7	...
2QZC-C4-HAE3	10:03:53.81 +00:36:05.7	19.54	21.27	4.8	1185	−16.04	42.52	26	9.9	...
2QZC-C4-HAE4	10:04:08.44 +00:43:09.8	19.66	20.95	3.7	600	−16.15	42.41	21	10.1	...
2QZC-C4-HAE5	10:03:54.01 +00:35:37.6	19.87	20.79	2.5	331	−16.31	42.25	14	10.1	...
2QZC-C4-HAE6	010:04:08.45 +00:34:58.3	19.89	>22.15	>3.8	>2913	−16.14	42.42	21	<9.6	...

^{a}The Hα flux (erg s^{-1} cm^{-2}) corrected for 33 per cent [N II] contribution to the measured flux.
^{b}The Hα luminosity (erg s^{-1}).
^{c}The attenuation-uncorrected SFR derived from the Hα luminosity (M$_{\odot}$ yr^{-1}).
^{d}The stellar mass estimated from the K-band magnitude by assuming a constant mass-to-light ratio from G08.
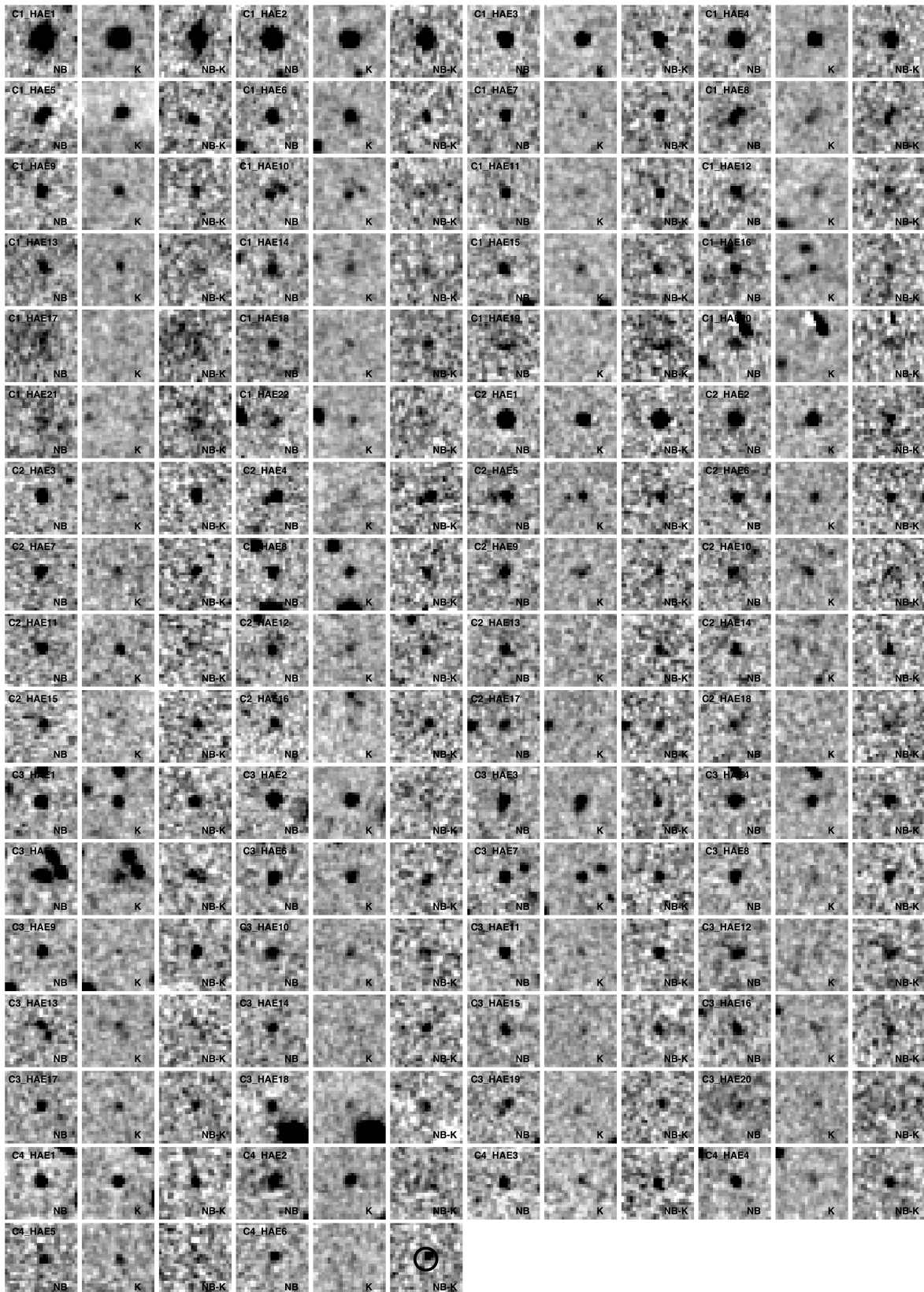
Figure A1. WFCAM thumbnail images of the emitter candidates in the 2QZ cluster and surrounding control fields. The size of the images is $10 \times 10 \, \mathrm{arcsec}^2$ ($\sim 80 \times 80 \, \mathrm{kpc}^2$). The circle in the bottom left-hand panel shows the size of the 3-arcsec aperture for photometry. The same magnitude range is used to display for all the images.

Table A2. Properties of the emitter candidates in the 0200+015 field (C3) and the control fields (C1, C2 and C4).

ID	Coordinate (J2000) ($^{h:m:s}$) ($^{\circ:\prime:\prime\prime}$)	H_2S1 (mag)	K (mag)	Σ	EW_{obs} (Å)	$\log F^a_{H\alpha}$ (cgs)	$\log L^b_{H\alpha}$ (cgs)	$SFR^c_{H\alpha}$	M^d_*	Note
0200-C3-HAE1	2:02:42.99 +01:49:10.8	16.48	18.30	55.9	1369	−14.81	43.76	451	11.1	HzRG
0200-C3-HAE2	2:02:50.22 +01:48:53.3	16.57	18.01	46.5	760	−14.89	43.68	375	11.2	NLAGN
0200-C3-HAE3	2:02:37.68 +01:44:33.2	18.19	19.43	9.6	557	−15.57	42.99	78	10.7	*BzK*
0200-C3-HAE4	2:02:37.36 +01:48:22.2	18.47	19.50	6.7	397	−15.73	42.84	54	10.6	*BzK*
0200-C3-HAE5	2:03:01.04 +01:52:09.9	18.85	19.70	4.2	288	−15.93	42.63	34	10.6	...
0200-C3-HAE6	2:02:46.98 +01:47:54.2	19.08	20.69	4.8	984	−15.87	42.69	39	10.2	*BzK*
0200-C3-HAE7	2:02:19.37 +01:55:39.8	19.13	20.13	3.6	375	−16.00	42.56	29	10.4	*BzK*
0200-C3-HAE8	2:02:24.55 +01:56:06.4	19.18	20.23	3.5	411	−16.00	42.56	29	10.4	...
0200-C3-HAE9	2:03:02.81 +01:49:20.5	19.35	20.15	2.6	265	−16.15	42.42	21	10.4	*BzK*
0200-C3-HAE10	2:02:51.92 +01:50:02.9	19.36	20.19	2.6	280	−16.14	42.42	21	10.4	*BzK*
0200-C3-HAE11	2:02:34.33 +01:44:58.9	19.47	20.57	2.8	442	−16.11	42.45	22	10.2	*BzK*
0200-C1-HAE1	2:01:03.23 +01:20:09.7	17.74	18.29	8.5	155	−15.62	42.94	69	11.1	...
0200-C1-HAE2	2:01:21.56 +01:24:45.0	18.32	18.58	2.6	61	−16.13	42.43	21	11.0	...
0200-C1-HAE3	2:00:36.54 +01:20:18.0	18.69	19.71	5.4	387	−15.82	42.74	44	10.6	...
0200-C1-HAE4	2:01:06.09 +01:23:30.8	18.73	20.09	6.1	664	−15.77	42.80	49	10.4	...
0200-C1-HAE5	2:00:38.81 +01:22:56.7	18.94	20.00	4.4	409	−15.91	42.65	35	10.5	...
0200-C1-HAE6	2:00:36.58 +01:19:53.7	19.08	20.36	4.3	590	−15.92	42.65	35	10.3	...
0200-C1-HAE7	2:00:57.57 +01:19:39.2	19.11	21.05	5.0	1635	−15.85	42.71	41	10.0	...
0200-C1-HAE8	2:00:43.94 +01:26:14.8	19.18	21.06	4.7	1485	−15.88	42.68	38	10.0	...
0200-C1-HAE9	2:00:33.53 +01:21:28.7	19.19	20.48	3.9	602	−15.96	42.60	32	10.3	...
0200-C1-HAE10	2:01:05.81 +01:23:50.3	19.23	21.63	4.9	3931	−15.87	42.70	39	9.8	...
0200-C1-HAE11	2:00:40.04 +01:19:22.0	19.35	20.88	3.7	863	−15.99	42.57	30	10.1	...
0200-C1-HAE12	2:01:07.72 +01:28:22.6	19.41	>21.75	>4.1	>3438	−15.94	42.62	33	<9.8	...
0200-C2-HAE1	2:03:08.25 +01:28:18.1	16.44	17.26	37.6	273	−14.98	43.58	303	11.5	...
0200-C2-HAE2	2:02:16.71 +01:30:06.7	17.99	18.59	7.3	176	−15.69	42.87	59	11.0	...
0200-C2-HAE3	2:02:52.26 +01:29:33.7	18.16	18.77	6.3	178	−15.75	42.81	51	10.9	...
0200-C2-HAE4	2:02:50.60 +01:24:55.1	18.51	19.57	6.6	417	−15.73	42.83	53	10.6	...
0200-C2-HAE5	2:02:52.81 +01:23:00.1	18.83	19.84	4.8	385	−15.87	42.69	39	10.5	...
0200-C2-HAE6	2:02:51.23 +01:30:57.2	18.85	19.97	4.9	456	−15.86	42.70	40	10.5	...
0200-C2-HAE7	2:02:46.26 +01:21:46.2	18.89	20.90	6.2	1839	−15.76	42.81	50	10.1	...
0200-C2-HAE8	2:03:00.80 +01:27:05.4	18.93	19.45	2.7	144	−16.12	42.45	22	10.7	...
0200-C2-HAE9	2:03:05.95 +01:28:22.9	19.17	20.61	4.2	762	−15.93	42.64	34	10.2	...
0200-C2-HAE10	2:02:51.75 +01:24:21.8	19.19	20.14	3.3	344	−16.04	42.53	27	10.4	...
0200-C2-HAE11	2:02:19.56 +01:30:54.0	19.21	20.54	3.9	639	−15.96	42.60	31	10.2	...
0200-C2-HAE12	2:02:19.72 +01:21:32.2	19.28	20.90	4.0	998	−15.95	42.61	32	10.1	...
0200-C2-HAE13	2:02:40.64 +01:30:18.2	19.41	>21.75	>4.1	>3445	−15.94	42.62	33	<9.8	...
0200-C2-HAE14	2:02:20.53 +01:18:16.1	19.44	20.45	2.7	384	−16.12	42.44	22	10.3	...
0200-C2-HAE15	2:02:16.49 +01:29:17.8	19.45	20.65	3.0	521	−16.08	42.48	24	10.2	...
0200-C2-HAE16	2:03:04.90 +01:29:38.8	19.47	21.12	3.4	1046	−16.02	42.54	27	10.0	...
0200-C4-HAE1	2:01:04.87 +01:50:43.6	17.41	17.65	5.6	55	−15.80	42.76	46	11.4	...
0200-C4-HAE2	2:00:57.44 +01:50:06.2	17.91	18.20	4.2	69	−15.93	42.63	34	11.2	...
0200-C4-HAE3	2:00:51.42 +01:45:56.2	18.18	18.55	4.2	94	−15.93	42.63	34	11.0	...
0200-C4-HAE4	2:00:53.01 +01:47:18.6	18.43	18.71	2.6	68	−16.13	42.43	21	11.0	...
0200-C4-HAE5	2:01:12.56 +01:45:14.7	18.72	19.74	5.3	388	−15.83	42.73	43	10.6	...
0200-C4-HAE6	2:00:47.83 +01:44:55.2	19.02	19.56	2.6	154	−16.13	42.43	21	10.6	...
0200-C4-HAE7	2:01:07.59 +01:44:34.1	19.24	20.87	4.2	1012	−15.93	42.63	34	10.1	...
0200-C4-HAE8	2:01:05.52 +01:48:03.1	19.27	21.15	4.3	1509	−15.92	42.65	35	10.0	...
0200-C4-HAE9	2:01:05.89 +01:48:13.6	19.37	20.59	3.2	537	−16.04	42.52	26	10.2	...
0200-C4-HAE10	2:00:48.00 +01:50:10.0	19.45	20.38	2.5	331	−16.15	42.42	21	10.3	...
0200-C4-HAE11	2:00:51.62 +01:47:20.2	19.46	20.77	3.1	617	−16.07	42.50	25	10.1	...
0200-C4-HAE12	2:00:55.98 +01:44:36.2	19.50	20.50	2.6	378	−16.14	42.42	21	10.2	...

[a]The Hα flux (erg s^{-1} cm^{-2}) corrected for 33 per cent [N ɪɪ] contribution to the measured flux.
[b]The Hα luminosity (erg s^{-1}).
[c]The attenuation-uncorrected SFR derived from the Hα luminosity (M$_\odot$ yr^{-1}).
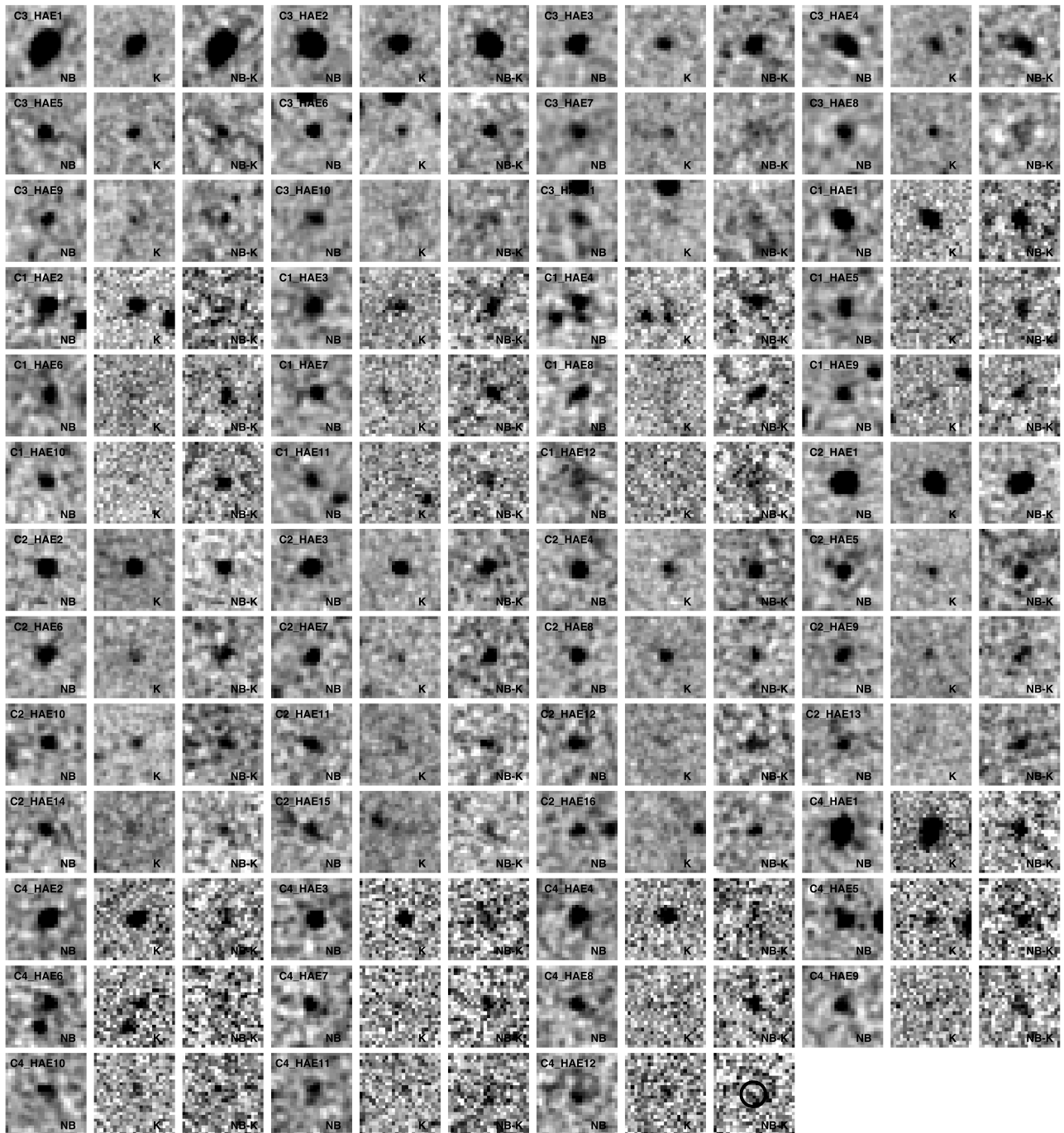[d]The stellar mass estimated from the K-band magnitude by assuming a constant mass-to-light ratio from G08.

Figure A2. WFCAM thumbnail images of the emitter candidates in the 0200+015 and surrounding control fields. The size of the images is $10 \times 10\,\mathrm{arcsec}^2$ ($\sim 80 \times 80\,\mathrm{kpc}^2$). The circle in the bottom left-hand panel shows the size of the 3-arcsec aperture for photometry. The same magnitude range is used to display for all the images.

Table A3. Properties of the emitter candidates in the SSA 13 (C1) and the control fields (C2, C3 and C4).

ID	Coordinate (J2000) (^{h}:^{m}:^{s}) ($^{\circ}$:$'$:$''$)	H_2S1 (mag)	K (mag)	Σ	EW_{obs} (Å)	$\log F^a_{H\alpha}$ (cgs)	$\log L^b_{H\alpha}$ (cgs)	$SFR^c_{H\alpha}$	M^d_*	Note
SSA13-C1-HAE1	13:12:27.80 +42:42:26.6	17.76	17.99	2.6	53	−15.95	42.61	32	11.3	...
SSA13-C1-HAE2	13:12:36.58 +42:40:02.5	18.26	19.04	4.5	254	−15.72	42.84	55	10.8	*BzK*
SSA13-C1-HAE3	13:12:42.53 +42:41:56.0	18.68	19.31	2.6	187	−15.95	42.61	32	10.7	*BzK*
SSA13-C1-HAE4	13:13:07.72 +42:34:41.0	18.71	19.81	3.7	445	−15.80	42.76	45	10.5	*BzK*
SSA13-C1-HAE5	13:12:10.36 +42:43:10.6	18.81	19.64	2.8	279	−15.92	42.64	35	10.6	*BzK*
SSA13-C1-HAE6	13:11:59.75 +42:42:53.3	18.98	20.14	3.0	490	−15.90	42.66	36	10.4	*BzK*
SSA13-C2-HAE1	13:14:44.24 +42:35:13.7	18.84	19.94	3.3	445	−15.86	42.70	40	10.5	...
SSA13-C2-HAE2	13:15:04.66 +42:39:44.0	18.92	19.83	2.7	322	−15.94	42.62	33	10.5	...
SSA13-C2-HAE3	13:15:21.66 +42:46:29.0	18.97	21.11	3.9	2331	−15.78	42.78	48	10.0	...
SSA13-C3-HAE1	13:15:03.25 +43:01:42.6	18.15	19.28	6.2	462	−15.58	42.98	76	10.7	...
SSA13-C3-HAE2	13:15:15.31 +43:09:52.7	18.32	18.71	2.5	100	−15.97	42.59	31	11.0	...
SSA13-C3-HAE3	13:15:13.54 +43:08:30.1	18.39	18.93	3.0	150	−15.89	42.67	37	10.9	...
SSA13-C3-HAE4	13:15:21.67 +43:06:01.3	18.49	19.61	4.6	457	−15.71	42.85	56	10.6	...
SSA13-C3-HAE5	13:14:22.61 +43:04:44.9	18.78	19.49	2.6	219	−15.96	42.61	32	10.7	...
SSA13-C4-HAE1	13:12:39.90 +43:12:11.9	17.24	17.63	6.7	99	−15.55	43.02	82	11.4	...
SSA13-C4-HAE2	13:11:58.12 +43:06:47.3	18.24	18.71	3.1	124	−15.88	42.68	38	11.0	...
SSA13-C4-HAE3	13:12:26.80 +43:01:46.4	18.86	19.65	2.6	260	−15.96	42.61	32	10.6	...
SSA13-C4-HAE4	13:12:45.44 +43:13:32.7	18.89	20.39	3.7	840	−15.80	42.76	45	10.3	...
SSA13-C4-HAE5	13:12:10.09 +43:07:36.8	18.89	19.94	3.0	408	−15.89	42.67	37	10.5	...
SSA13-C4-HAE6	13:12:22.13 +43:01:34.0	18.98	19.99	2.7	382	−15.94	42.63	33	10.5	...

[a] The Hα flux (erg s^{-1} cm^{-2}) corrected for 33 per cent [N II] contribution to the measured flux.
[b] The Hα luminosity (erg s^{-1}).
[c] The attenuation-uncorrected SFR derived from the Hα luminosity (M$_\odot$ yr^{-1}).
[d] The stellar mass estimated from the K-band magnitude by assuming a constant mass-to-light ratio from G08.
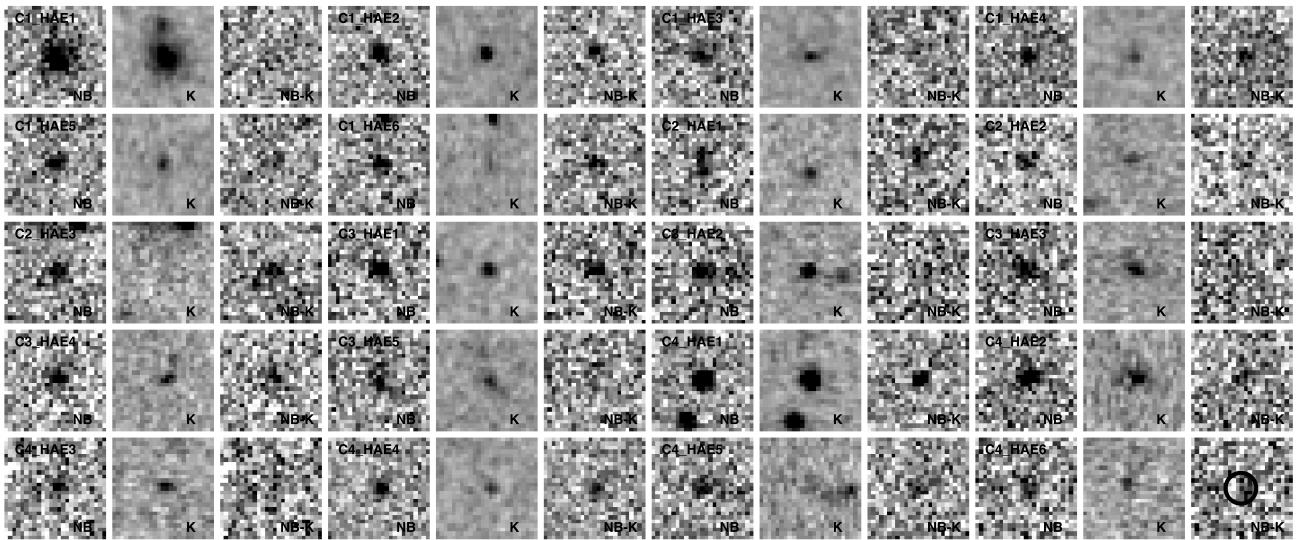

Figure A3. WFCAM thumbnail images of the emitter candidates in the SSA 13 and surrounding control fields. The size of the images is $10 \times 10\,\mathrm{arcsec}^2$ ($\sim 80 \times 80\,\mathrm{kpc}^2$). The circle in the bottom left-hand panel shows the size of the 3-arcsec aperture for photometry. The same magnitude range is used to display for all the images.

This paper has been typeset from a TEX/LATEX file prepared by the author.